sustainability

MDPI

Article

Design and Analysis of DFIG-STATCOM Coordinated P2P Grid Connected System Using RMSProp

R. R. Hete [1], Sanjay Kumar Mishra [1], Ritesh Dash [2,*], Kalvakurthi Jyotheeswara Reddy [2], Vivekanandan Subburaj [3] and Dhanamjayulu C [4,*]

[1] Department of Electrical Engineering, G. H. Raisoni University Amravati, Amravati 444701, India
[2] School of Electrical and Electronics Engineering, REVA University, Benagaluru 560064, India
[3] Department of Electrical Engineering, National Institute of Technology Silchar, Silchar 788010, India
[4] School of Electrical Engineering, Vellore Institute of Technology, Vellore 632014, India
* Correspondence: rdasheee@gmail.com (R.D.); dhanamjayulu.c@vit.ac.in (D.C.)

Abstract: This research work establishes a relationship between STATCOM and DFIG wind turbines in a transmission network for coordinated operation during grid disturbances. A change in wind gust also produces a variable output nonlinearly, thereby making the system unstable. Assuring bus voltage and proper balance of load angle in all the connected generating stations becomes challenging. Therefore, increasing voltage security at all the lines and further enhancing system stability leads to the placement of STATCOM at the proper location in the transmission line. Appropriate coordinated control of STATCOM and DFIG can lead to adequate power flow in the system. This research includes a multi-objective optimization problem for properly tuning the PI- controller. The voltage at the controlled bus, low-frequency oscillating waveforms, and real power available at the bus under pre-fault and post-fault conditions are identified as objective function parameters. To avoid the overgrowth of error inside the search space due to lack of normalization, this method uses the RMSProp algorithm for proper convergence in the state vector. The coordinated control action has been investigated in the different shunt fault conditions. Again, to enhance the system stability, low voltage ride-through capability has been thoroughly verified using Matlab software.

Keywords: DFIG; STATCOM; deep learning; RMSProp; FPA; ANFIS

Citation: Hete, R.R.; Mishra, S.K.; Dash, R.; Jyotheeswara Reddy, K.; Subburaj, V.; C, D. Design and Analysis of DFIG-STATCOM Coordinated P2P Grid Connected System Using RMSProp. *Sustainability* **2022**, *14*, 15105. https://doi.org/10.3390/su142215105

Academic Editor: Miguel Carrión

Received: 28 September 2022
Accepted: 10 November 2022
Published: 15 November 2022

1. Introduction

As time goes by, there has been an increase in load demand, and generation capacity has also increased. In recent years, renewable energy sources like hydro, solar, wind, geothermal, and tidal, which can generate energy, have been getting immense amounts of attention. Wind power generation now has several benefits. They are cheap in the long run and are environmentally friendly. Therefore, wind power generation is being incorporated at a fast pace into power systems all around the world. The DFIG-based wind turbines can be installed at a lower cost than conventional wind turbines. It holds a certain amount of efficiency when transferring energy at a different wind speed, with the advantage of having a converter that has a small capacity. DFIG-based wind turbines are used in many wind farms because they have active and reactive power control and variable speed constant frequency operating characteristics [1,2].

One drawback of the DFIG-based wind turbines is that they show technical challenges, which ask us to consider the stability of the turbine voltage regulation and the power quality issues. Still, the positioning of the wind turbine farms has many economic and environmental advantages. However, the wind speed and strength keep changing in nature frequently, and these changes cause wind power generation trouble. Therefore, this leads to grid outages, which includes a constraint that the wind speed and strength should be 5 to 15 RPM. Beyond these parameters, it may cause severe issues with generation; another challenge added to adjusting the energy supply to the demand [3,4].

In traditional power plants, the requirement for reactive power control is a grid code. As for wind farms, voltage control is needed to maintain effective reactive power control. Wind farms should be connected to the grid during fluctuations in wind forms and the grid exchange reactive powers. The grid will inject and take out the reactive power depending on the power generation and the grid's demand. The TSO determines the quantity and the exchange rate. The active power regulation highlights the differences between active power and actual output power and must be kept following the grid code's voltage and frequency diagram under the TSO criteria. Then, the control can be set. In grid code, various ways are given for power and frequency characteristics [5,6].

If reactive power absorption correction is successful on long transmission lines, it can increase the steady-state stability, improve the natural characteristics of transmission lines, give active power to load, and give sufficient control over the timing of the voltage curve. Reactive power compensation equipment gives immense compensation, helping to improve system stability. This equipment includes static reactive power compensators, bypass capacitors, and STATCOMS. The complexity increases as we connect DIFG-based wind power and STATCOM-connected grid operation [7]. The change of wind speed is on and off and is not constant at all. Due to these uncontrollable changes in the wind speed, there are fluctuations in the active and reactive power. A combination of a fact device, mostly STATCOM, and a DFIG is used to solve this issue. STATCOMS has different applications for controlling power, including reactive power. It helps to lower the changes and fluctuations of energy.

Here, we studied if there was an increase in transient stability in wind power generation by a DFIG with the applications of STATCOM. In simple words, STATCOMS can be said to be a device that is fast-acting from the facts family, which should be connected to a system in a shunt for compensation, capable of providing and getting reactive power from the grid [8,9]. The output of a STATCOM device can be changed to control the specific power system performance measures. According to Shaigan M. et al., there is an increase in static voltage stability using STATCOM, and an examination of whether improving stability in active and reactive losses is also done. Shaigan M. et al. have also accurately proved that the devices could enhance static stability and be applied in primary and load systems. The dynamics of the system have less effect on the stability of the voltage; therefore, the static technique can be applied to examine the possibilities of getting a balance at a point limited by the system's specific boundaries [10,11].

FACT devices have higher installation costs. Therefore, it is not economically feasible to provide all the buses. As a result, the power system requires an ideal STATCOM placement. As mentioned earlier in this paragraph, system performance is less dependent on dynamic performance. Therefore, a robust static investigation of network steady-state may lead to better solutions. The most challenging aspect of determining the proper placement of a STSTCOM is often calculating the non-linear and complex energy flow equations. Various optimization strategies have been described in the literature to solve the equations [12]. This includes optimal power flow (OPF), heuristic optimization methods, continuous power flow, loss prediction sensitivity analysis, effective cost analysis, and probabilistic algorithms. Genetic algorithms (GA), particle swarm optimization (PSO), evolutionary search, and harmonic search are some subcategories.

The authors in [13,14] proposed a STATCOM-DFIG connection, establishing coordination between the wind turbine and their STATCOM. In another article, the authors mentioned heuristic dynamic programming that establishes a bi-directional relationship between the wind turbine and STATCOM based on the voltage drop across the link. Tarevi et al., using a GA-based optimization approach, gave the SVC a discrete-time domain to distribute the load. Distributor feeder unbalanced loading usually serves two purposes. Firstly, the velocity of the unbalanced load varies over time and is distributed among the feeders. Within seven days, the imbalance between actual feeder samples was investigated using pre-developed software, and the proposed algorithm was tested on a 27-bath test system. They calculated total active power compensation. This result shows that the algorithm

has accurately optimized the location, size, and design of FACTS devices. Preethi et al. proposed using various FACTS devices to improve grid voltage stability. This work uses the classical Newton–Raphson method for load flow analysis under various load conditions. Finally, the authors in [15] proposed an AI-GA-based congestion management solution that integrates FACTS devices into deregulated power systems. There are two types of methods to ease congestion. Firstly, we need a better location due to the high cost of FACTS equipment. Since the objective function is non-linear, GA techniques are required [15]. The main reason for using the PSO method is to create computer models that simulate social behavior, which are also very successful in system optimization. This phenomenon is used to find optimal solutions to various mathematical optimization problems. PSO can be used to solve a variety of real-world optimization challenges. PSO can also be reliable and easy.

PSO is also valuable in various energy-related industries. In an advanced method for optimizing particle swarms. Ravi et al. proposed their improved PSO method for designing FACTS devices to reduce power system losses and improve voltage distribution. That algorithm selects SVCs and STATCOMs for their optimal location and size within the power system. In the STATCOM block of today's infrastructure, advanced PSO technology provides optimal settings, ideal site size, and control settings. An IEEE 30 bus test system was used as an example to demonstrate this concept. Calculations show the reliability of the power grid and the efficiency of this concept. Calculations also show that the reliability of the power grid and the efficiency of this technology have improved. They proposed a PSO program to improve voltage stability after faults in the most critical lines of the power system by optimizing SVC placement and re-sizing [16].

This new method of evaluating the severity of the line disturbances takes into account improved reactive power generation. The author [17] presented a PSO method for determining the optimal position and size of SVC to minimize transmission loss considering the cost function. Their SVC was chosen as the compensating device in this process. Pilot studies highly suggested their SVC placement. The performance of this method was tested using the IEEE 26 bus test system. Another PSO-based approach minimizes transmission loss considering voltage distribution and cost function. SVC was selected as the compensating driver and was developed as a source for computer iterations compiled on the system bus. The researcher [18] presented their PSO technique for determining the optimal location of the FACTS device while reducing its installation cost and increasing system load capacity. The thermal limits of the bath were considered a limitation to obtaining an appropriate placement. This method used SVC, TCSC, and UPFC.

An altered simulation measure-up was recommended [19–21] as an explanation to the transmission line congestion issue. Concerning placing the facts devices on an appropriate bus and determining the size of the fact's devices, the suggested technique was evaluated. To reduce the load on the power supply, this appeal used a controlled series capacitor synchronized by a thyristor and a static variable compensator. Further, the suggested approach can review the power system's economic limitations and the amount of reactive power intake into account [22–24]. Related to single-objective optimization, multi-objective optimization issues can be characterized as priority-based discernment that lets users take any method of action based on its acceptability from an economic perspective [25,26]. In contrast to random iteration, the normalized algorithm proposed can yield superior outcomes because it avoids local minima.

The STATCOM shunt compensator is mostly used in this article to optimize the voltage profile and power transfer accuracy. It optimizes the overall system transient, dynamic, and voltage regulation stability [27]. A multi-objective optimization issue regarding the vital role of reactive power between a wind farm and STATCOM is the main goal of this research [28,29]. The converter's lower operating capabilities determine the capability to withstand voltage swings. Capacity utilization may be maximized with lower voltage fluctuations [30–33]. The variation in voltage variations could be characterized as a multi-objective function as an outcome. The second main objective presented in this approach is to analyze network properties in post-fault conditions using the transient severity index.

Reactive power, the starting state variable, impacts this vertical function [34]. Influential decision-makers organize reactive power management between STATCOM and wind power plants, utilizing adaptive neuro-fuzzy inference algorithms [35,36].

Through the external controller interface and by utilizing the voltage output and reactive power, STATCOM and the wind farm can be operated. Multi-criteria optimization issues are generated by stochastic methods and are analyzed by an adaptive neuro-fuzzy inference system. This model combines doubly-fed induction generators and STATCOM, while doubly-fed motors are a common characteristic of wind farms [37]. It is crucial to remember that the suggested control approach applies to all models of wind turbines, not just DFIGs. However, the station can be modified by a static compensator VAR [38,39].

2. Problem Identification and Modelling of DFIG-STATCOM

The power output of the wind turbine can be characterized by the function of three inputs, such as wind velocity, wind gust, power generator, and transmission and distribution. Again, the power quality can also be evaluated in terms of voltage sag, well, and harmonics [40]. Generally, the wind generator introduces power quality disturbance into the distribution network. One of the simple methods of running a wind generating system is to use the induction generator connected directly to the grid system. The induction generator has inherent advantages of cost effectiveness and robustness. This requires reactive power for magnetization of induction motor in order to inject real power into the grid. This requires a regulated voltage control system to control the production of active power at the converter terminal [41,42].

During normal steady-state operating conditions, the slip and speed fluctuations of an induction generator are minimal. The reactive power absorbed by the machine is minimal under this scenario but increasing the load and power will likewise increase the motor's *slip* and reactive power consumption. The equations for stator voltage and flux can therefore be written as follows

$$\begin{cases} V_s = R_s L_s + \frac{d\varnothing_s}{dt} \\ \varnothing_s = L_s I_s + L_m Ir \end{cases} \quad (1)$$

Additionally, the equations rotor side voltage and fluxes can be written as

$$\begin{cases} V_r = R_r I_r + \frac{d\varnothing_r}{dt} - j\omega_m \varnothing_r \\ \varnothing_r = L_r I_r + L_m I_s \end{cases} \quad (2)$$

From the above two equations, the rotor and stator voltage become

$$\begin{cases} V_r = R_r I_r + sj\omega_s L_{\sigma r} + sj\omega_s L_m (I_r + I_s) \\ V_s = R_s I_s + j\omega_s L_{\sigma r} I_s + j\omega_s L_m (I_r + I_s) \end{cases} \quad (3)$$

In the above equation '*s*' represents the slip of the system. From the above equation number (3), the active power of stator and rotor becomes

$$\begin{cases} P_s = \frac{3}{2} Re(V_s.I_s) = \frac{3}{2} R_s (I_s)^2 + \frac{3}{2} \omega_s L_m R_s (j(I_r.I_s)) \\ Q_S = \frac{3}{2} Re(V_r.I_r) = \frac{3}{2} R_r (I_r)^2 + \frac{3}{2} s\omega_s L_m R_s (j(I_s.I_r)) \end{cases} \quad (4)$$

Further three phase line voltage can be written as

$$\begin{cases} V_{ag} = I_a R_a + L\frac{dI_a}{dt} + V_{fa} \\ V_{bg} = I_b R_b + L\frac{dI_b}{dt} + V_{fb} \\ V_{cg} = I_c R_c + L\frac{I_c}{dt} + V_{fc} \end{cases} \quad (5)$$

From Equation (5), deriving the *d*-*q* component

$$\begin{cases} V_d = I_d R + L\frac{dI_d}{dt} - L\omega I_q + V_{fd} \\ V_q = I_q R + L\frac{dI_q}{dt} + L\omega I_d + V_{fd} \end{cases} \quad (6)$$

From the above equation, three different contradicting features can be pointed out: correction factor, decoupling item, and voltage compensation. In this article, voltage compensation factor is used in the form of a STATCOM [43]. The equation for reference current control loop becomes

$$\begin{cases} I_d^* = \frac{P^* V_{fd} + Q^* V_{fd}}{V_{fd}^2 + V_{fq}^2} \\ I_q^* = \frac{P^* V_{fq} - Q^* V_{fd}}{V_{fd}^2 + V_{fq}^2} \end{cases} \tag{7}$$

For getting unity power factor, $I_q^* = 0$ and therefore

$$\theta = \tanh \frac{V_\beta}{V_\alpha} \tag{8}$$

Power converter voltage i.e., STATCOM voltage, is proportional to DC voltage, and therefore

$$\begin{cases} V_d = m V_{dc} \cos(\theta) \\ V_q = m V_{dc} \sin(\theta) \end{cases} \tag{9}$$

Hence, using Equations (6), (8), and (9), the power balance equation becomes

$$\begin{cases} P = \frac{3}{2}\left(V_d I_d + V_q I_q\right) \\ i_{dc} = \frac{3}{2} m \left(i_d \cos(\theta) - i_q \sin(\theta)\right) \end{cases} \tag{10}$$

3. Problem Formulation and Solution Methodology

In the stated research area, the coordinated control among DFIG and STATCOM requires optimization of PI-controller parameters such as proportional gain (K_p) and integral gain (K_i) in response to the transient disturbance in the power system network [44]. The active control of power flow between these two units requires time-dependent boundary condition with PDE constraints for optimization. The time-dependent PDE constraints can be addressed by the Navier–Stokes system by converting the first order system into the Karush–Kuhn–Tucker (KKT) system. Let us consider the single input and single output (SISO) system, as shown in Figure 1b.

The transfer function for Figure 1b becomes

$$G(s) = \frac{N(s)}{D(s)} \tag{11}$$

And

$$C(s) = K_p + \frac{K_i}{s} = \frac{K_p s + K_i}{s} \tag{12}$$

By combining (11) and (12) and solving the characteristics equation, the proportional and integral constant can be written as

$$K_p = \frac{\omega^2 D_0\left(-\omega^2\right) N_0\left(-\omega^2\right) + D_e\left(-\omega^2\right) N_e\left(-\omega^2\right)}{-\left(\omega^2 N_0^2(-\omega^2)\right) + N_e^2((-\omega^2))} \tag{13}$$

And that of

$$K_I = \frac{\omega^2 D_e\left(-\omega^2\right) N_0\left(-\omega^2\right) - \omega^2 D_0\left(-\omega^2\right) N_e\left(-\omega^2\right)}{-\left(\omega^2 N_0^2(-\omega^2)\right) + N_e^2((-\omega^2))} \tag{14}$$

The optimized value for K_p and K_i, as shown in Equations (13) and (14), can be derived by using the Navier–Stokes equation, such that the

$$\frac{Cost\ towards\ optimization}{Cost\ towards\ Iteration} \leq K \tag{15}$$

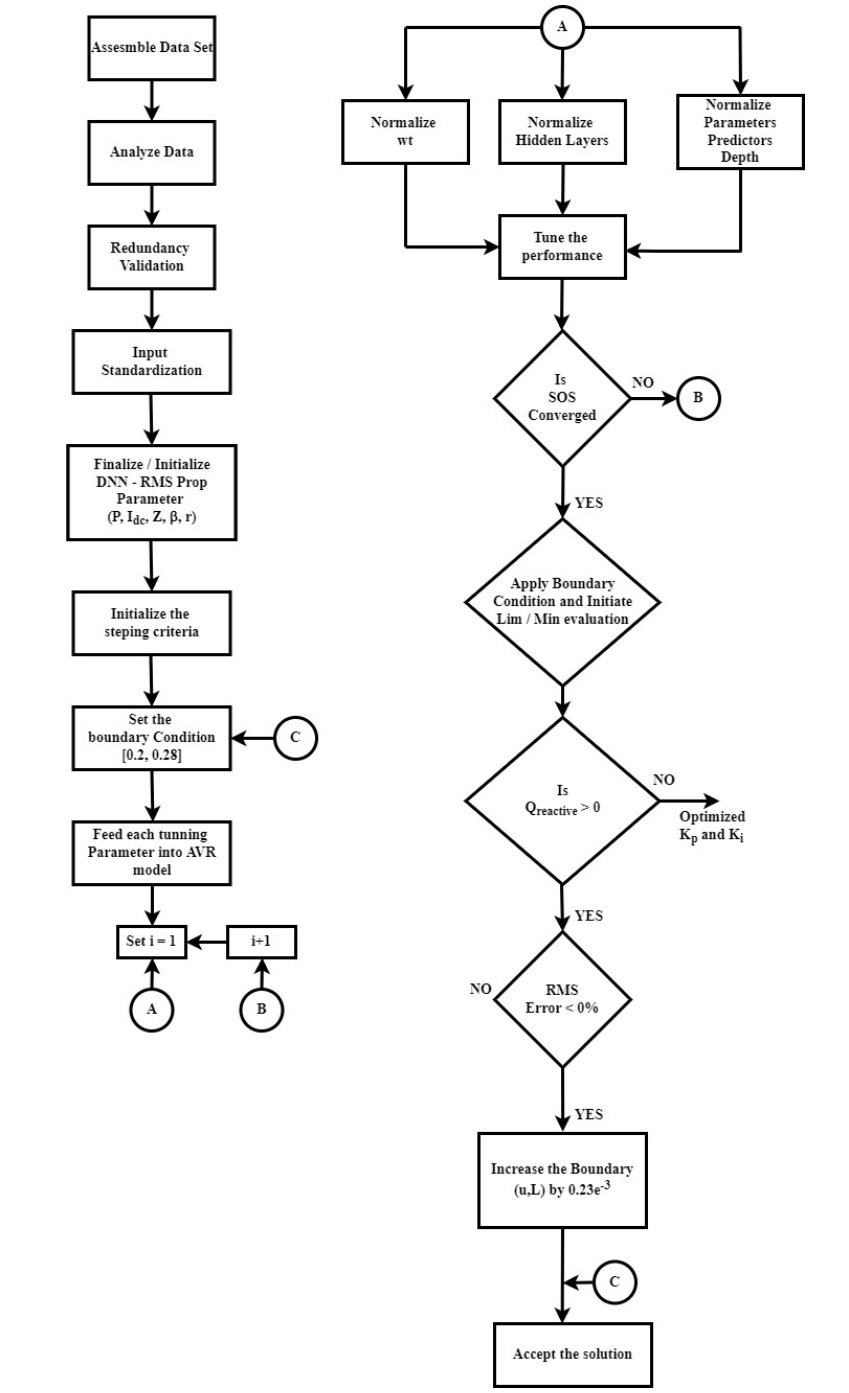

Figure 1. (**a**) Parameter-tuning flowchart using RMSProp model. (**b**) SISO model of the proposed system.

In Equation (15), K represents the performance evaluator. The system becomes moderate for $K > 0$, which implies that the optimization is convergable [45]. Based on the facts derived from Equation (5), let us consider the optimization for optimal control of active power as the objective, as stated under Section 2 in Equation (10).

$$J(P, i_{dc}) := \frac{1}{2}\|p - z\|^2_{L^2(Q)} + \frac{\beta}{2}\|i_{dc}\|^2_{L^2(Q)} + \frac{\sigma}{2}\|p(t) - z(t)\|^2_{L^2(\Omega)} \rightarrow min! \tag{16}$$

$$s.t.$$

$$\begin{cases} p(t) - v.\Delta i_{dc} + p(t)\Delta p(t) + \nabla p_d = f(i_{dc}) \forall Q_{reactive} \\ -\nabla p = 0 \; \forall Q_{reactive} \\ P(0, \Delta p) = p^0 \forall \Omega_{impedance} \\ p = g(p) \forall T_{time-space} \end{cases} \tag{17}$$

Here $\Omega_{impedance} \subset R^d$, denotes the open bounded impedance. $\Omega_{impedance}$ has to be decided based on the filter parameter for the STATCOM. $Q_{reactive}$ shows the time boundary value of reactive constraints. i_{dc} is the control value as a function of direct and quadrature current and is the target variable for optimization. Based on KKT condition, the necessary condition for Equation (17) can be written as

$$\begin{cases} P_t - v.\Delta i_{dc} + p\Delta p + \nabla p_d = f(i_{dc}) \forall Q_{reactive} \\ -\nabla p = 0 \; \forall Q_{reactive} \\ \dot{P} = g(p) \; \forall \; T_{impedance} \\ p(0, \dot{\Delta p}) = p^0 \forall \Omega_{impedance} \end{cases} \tag{18}$$

Or

$$\begin{cases} -\lambda_t - v\Delta\lambda - p\Delta p + (\nabla \mathrm{p})^t \lambda + \nabla\zeta = \mathrm{p} - \mathrm{z} \; \forall Q_{reactive} \\ -\nabla \mathrm{p} = 0 \; \forall Q_{reactive} \\ \lambda = 0 \; \forall T_{time-space} \\ \lambda(t) = \Gamma(p(t) - z(t)) \; \forall \Omega_{impedance} \\ i_{dc} = \frac{-1}{\alpha}\lambda \; \forall Q_{reactive} \end{cases} \tag{19}$$

The primal and dual equation can be derived from Equations (18) and (19) as follows

$$\begin{cases} P_t - v.\Delta i_{dc} + p(t)\Delta p(t) + \nabla p_d = \frac{-1}{\beta}\lambda \\ -\nabla p = 0 \\ p\left(0, \dot{\Delta p}\right) = g(p_0) \end{cases} \tag{20}$$

Or

$$\begin{cases} -\lambda_t - v.\Delta i_{dc} - p\nabla\lambda + (\nabla \mathrm{p})^t \lambda + \nabla\zeta = p - z \\ -\nabla.\lambda = 0 \\ \lambda(t) = \Gamma(y(t) - z(t)) \end{cases} \tag{21}$$

Equations (20) and (21) represent the primal and dual equation. The time discretized equation, as derived from Equation (20), can be written as

$$\begin{cases} \frac{P_{k+1} - P_k}{\Delta t} - V\Delta i_{dc(k)} + P_{k+1}\Delta P_{k+1} + \nabla_{pd(k+1)} = \frac{-1}{\beta}\lambda_{k+1} \\ -\nabla.P_{k+1} = 0 \\ P_0 = P^0 \end{cases} \tag{22}$$

In Equation (22) the initial solution may not be conversable, so by applying the Navier–Stokes equation, Equation (22) can be reduced to

$$\begin{cases} \frac{1}{\Delta t}P_0 - v\Delta i_{dc0} + P_0\Delta P_0 + \nabla.P_{d0} = \frac{1}{\Delta t}P^0 - V\Delta i_{dc0} + P_0\Delta p^0 \\ -\nabla.P_0 = 0 \end{cases} \tag{23}$$

With reference to Equation (23), it is understood that the learning rate becomes slower because of unbounded solutions. Let f be a function on the space diagram P, where R $\bigcup$ {+∞} [46]. Let us consider the optimization problem to be

$$m = \inf\{ f(p_o)|_{p_o \in P} \tag{24}$$

From Equation (24), let the optimal solution be 'S'. According to Buttazo and Tomarelli model, the conditions which satisfy Equation (24) can be derived as based on the following assumption, such as

$$\begin{cases} H^0 \, f_\infty(p) \geq 0, \quad \forall \, p \in P \\ H^1 \, f_\infty(p) \leq -1, \quad \forall \, |p_0| \to +\infty \end{cases} \tag{25}$$

And

$$\frac{p_0}{\|p_0\|} \to \overline{p} \in \lfloor V, \;\; f_\infty(v) = 0 \tag{26}$$

Then a surface exists [D_n, $\zeta_n \in$ o] for large value of n. If it satisfies all the constraints at (25), then optimal set S is nonempty and H^0 and H^1 are satisfied. If f becomes coercive then solution H^0 and H^1 are also coercive. Therefore, the adagrade in deep-learning is required to solve coercive. However, it is a non-convex optimization, and the technique is not suitable from a convergence point of view. In order to avoid the overgrowth of $g(P_0)$ variable in the vector space, and due to lack of normalization, it is proposed to use "RMSProp" into the convergence algorithm with the state vector $g(P_0) = g(P_0)_{t-1} + gP_0^2$. Note that from a RMSProp optimization point of view, H^0 and H^1 must be converted into state space domain such as $\dot{m}_1$ and $\dot{m}_2$, with optimization function such as $f(i_d,i_q,V_{dc}) = \dot{m}_1 x + \dot{m}_2 y$. Here, x and y represent P_0 and V, respectively.

4. Bench Marking Model

The suggested method for DFIG-STATCOM coordinated control has been verified for the inner and outer fault zone. The ANFIS controller is used to regulate the DFIG-STATCOM coordination in Figure 2. To produce separate control action on the rotor and grid sides, two types of converters, converter on the rotor side (RSC) and converter on the grid side (GSC), were coupled back to back. In the current model, however, PI current controller based on an ANFIS has been implemented, with Vdc serving as a reference and regulated voltage reference quantities to rotor and grid side converters are Vr and Vgc, respectively, allowing these two converters to operate in a coordinated way indirectly. Wind side turbine gives DC quantity of reference, and other reference quantities such as frequency and voltage are supplied using PLL from the grid side converter.

The STATCOM consists of a DC supply governed by voltage and current reference parameters obtained from GSC. To demonstrate the controller's sturdiness, the model was compared to two distinct methodologies, as given below:

- Case-I: ANFIS tuned PI controller for achieving coordinated control of DFIG-STATCOM.
- Case-II: FPA tuned Gaussian PI Controller

4.1. Case-I

The input parameters for an ANFIS controller need to be set to change proportionately as per the process needs. At the start, choose two inputs to the controller that denote the output state (given by the object output). The output of PI controller is set as a target for the process of production and for the final stage of the neural network training and replicating model. Triangular membership functions are used as parameters. The in-feed and result variables of the controller are constructed using the five membership functions of NL, ZE, PL, NS, and PS. They are used as language variables. During training, these parameters are trained at intervals of 10 epoch. The fundamental PI controller, which is ANFIS-based for the suggested system, is shown in Figure 3. Standard PI controller is used here to process the parameters I_d and I_q. This output of the controller is given to the first layer, and it converts this to a crisp variable. Five membership functions (MFs) are employed in

the current model. Taking reference from MF, the back propagation technique was used to estimate various types of two weights (w1 and w2). The normalization property was utilized to turn the same into a second level of crisp variable. It is then converted back to initial physical variable at the end of layer 5 using addition operations.

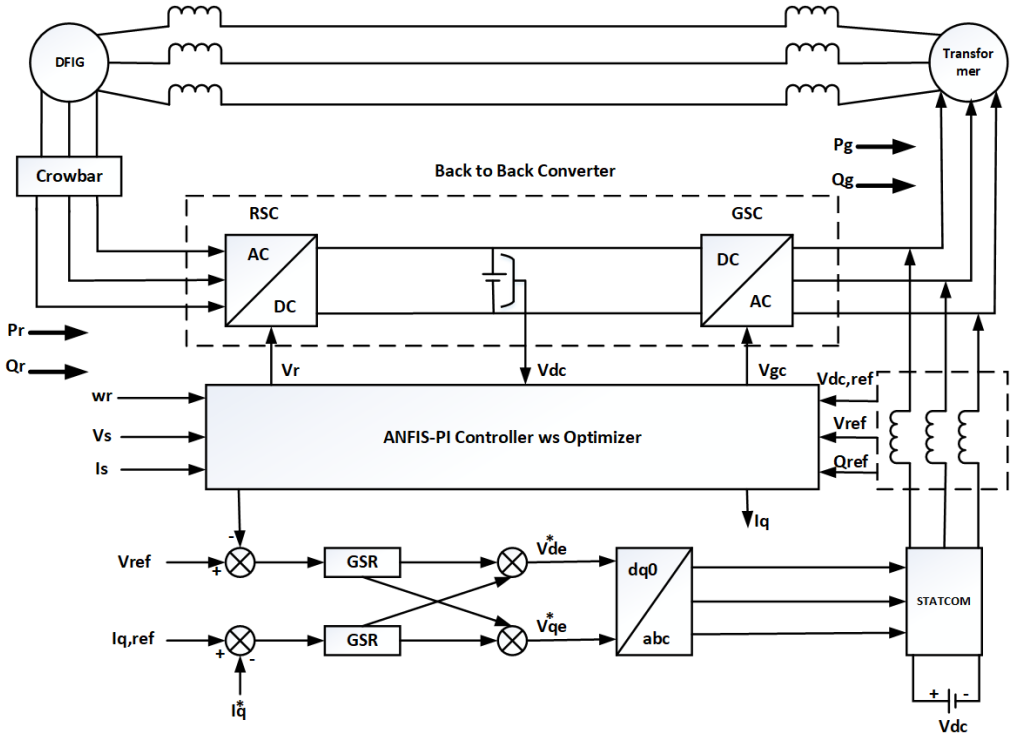

Figure 2. Coordinated control of DFIG-STATCOM with ANFIS controller.

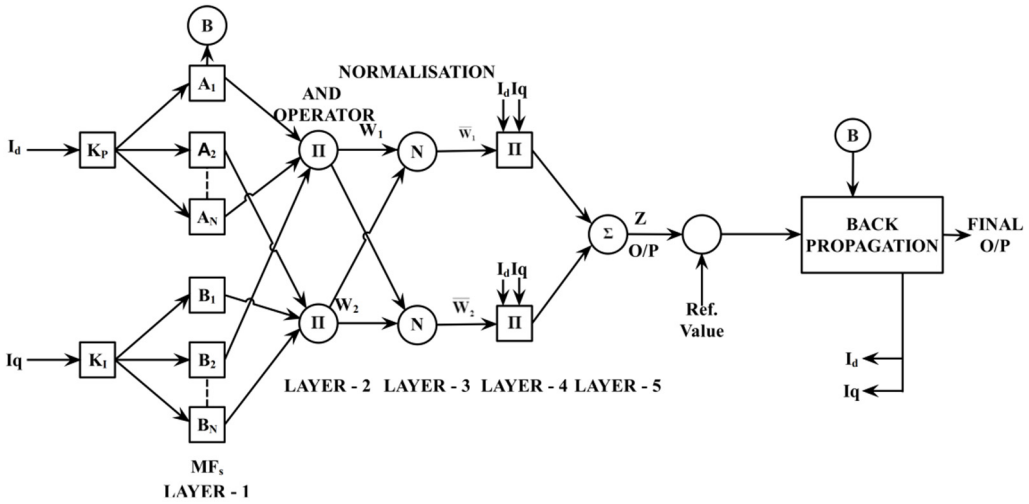

Figure 3. Architecture of basic ANFIS controller.

It is clear from the curve fitting application that the rule followed by all program agents is linear dependency. The rules of the Takagi–Sugeno fuzzy interference system, which is ANFIS based, were used to establish this. For this reason, to develop the rules in this paper, it has been used. ANFIS output is normally a linear mixture of input variables with some constant variables. Weight functions are commonly used to these linear combination variables. ANFIS controlled structures typically produce a sum average of input which is a flat weighted, turned into output as their final output. Sometimes, when the number of rules in a fuzzification process increases in the number of membership functions and

input, the system becomes more complicated and difficult to manage the variables within the limit. Sugeno-style methods (also known as Takagi–Sugeno) have inputs fuzzy and outputs crisp. The process is extremely effective when it comes to adaptive optimization, making it ideal for solving control problems. The following is a basic ANFIS structure with (z) as one output and x and y as two inputs, which can be written as follows:

Takagi–Sugeno fuzzy system follows the Rule table, and it is If and Then rules.

Rule-1 = If xx is X_1 and yy is Y_1 then function f1 = A_1xx + $b_1$xx + r1

Rule-2 = If xx is X_2 and yy is Y_2 then f2 = A_2xx + $b_2$xx + r2

For Layer 1

For each nodal point I in the present layer, the square node point functional parameter will be

O1, i = μX, i(xx) values for i here as (1, 2)

O1, i = μY, i(yy) values for i here as (1, 2)

For node I input here is denoted by X or layer-1 is mention here and linguistic informational weighted variable are expressed by "X" and "Y" exist at that node. Like membership values of triangular or Gaussian, here also two types of Linguistic variables can be used. Variables assigned to Layer-1 are named as premise parameters. Here, xx and yy represent the x set of input X and y represents the y set of input Y.

Layer 2

π is the node value for set Layer 2. Again, the output of Layer 2 is the product of all incomers.

O1, i = μA, i(xx) X μB, i(xx) here values of i as (1, 2). Strength rules of fuzzy logic can be seen from the fixed layer number 2 output.

Layer 3

For layer 3, the node level is N. It is expressed as ratio of fuzzy rules strength to the addition of strength of fuzzy rule tables.

O3, i = wi = $\frac{\text{wi}}{(\text{w1}+\text{w2})}$ for values of i as (1, 2)

The output of layer 3 indicates the normalized solution of fuzzy rules.

Layer 4

This layer is stated as adaptive fuzzy node. The nodal function for layer 4 is shown as

Oq, i = wifi = wi (p1xx + qiyy + ri)

Layer 5

Layer 5 output shows the summation of the average of linearly time-dependent input variable. For this layer number 5, the equation for the crisp output can be written as

Oc, i = Σwifi

Again, the above discussion shows that the ANFIS (adaptive neural fuzzy inference system) is identical to the fuzzy system-based type Takagi–Sugeno in all cases.

Calculating the difference between projected and actual output can be used to assess the ANFIS controller's efficiency. The kind of loss function employed in this article is sparse categorical cross entropy. In terms of its probability distribution, the layer output may be expressed as

$$h(p) = -logP\ (\sum \omega_i f_i) \tag{27}$$

Equation (27) can be expressed as follows, which shows the entropy for $h(p)$.

$$(p) = -\sum \omega P\ (\sum \omega_i f_i) logP\ (\sum \omega_i f_i) \tag{28}$$

A negative sign in Equation (28) indicates that positive or zero results always occur.

If for the output layer the probability distribution is 1, then Equation (14) gives zero output. Similarly, from Equation (27), it is clear that if there is single output, $h(p)$ will be minimum.

Optimized well-trained FIS file must be created for the fuzzy logic controller used in ANFIS, and ANFIS requires accurate data. As a result, the data must be obtained with the largest possible error [23]. Before processing FIS files, data verification is required. With this, data from the PI controller are checked. To achieve the best results, the variable

Id and Iq are derived from the PI controller's input and output. Figure 3 depicts the PI controller's inputs and outputs, which are given to the data inspector for error detection. Under error analysis, the error between output, input, and output of the neural network is displayed in Figure 4.

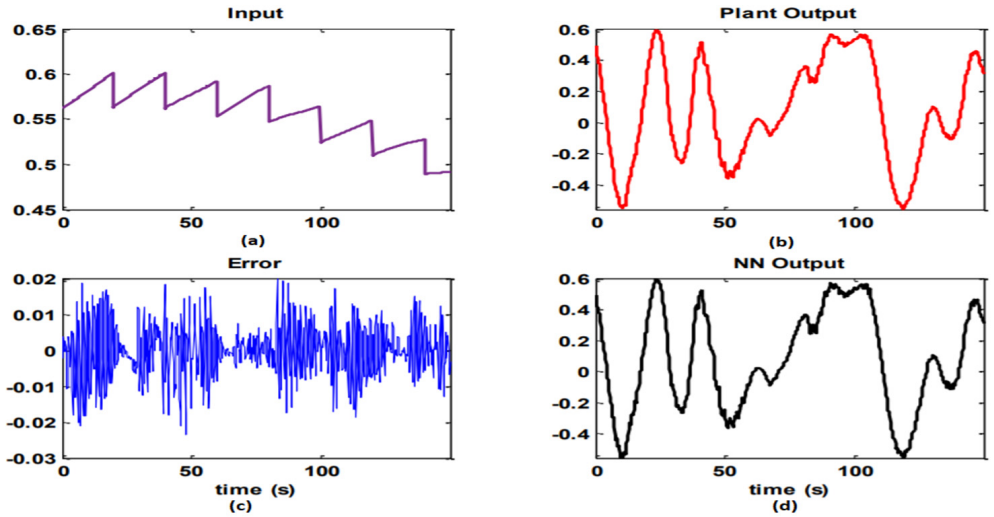

Figure 4. Training of data using neural network for sample 1, (**a**) plant input (*Idin*), (**b**) reference plant output (*Idout*,*ref*), (**c**) controller from actual output to ref. output, (**d**) ANFIS plant output (*Idout*,*act*).

The error displayed transient behavior owing to load variations after nearly 30 s. 0.012 to 0.012 is the usual range for error during 30 s, excluding for the transition state. For the algorithm of Levenberg–Marquardt, the overall throughput is 3.92×10^6, with 1.04×10^5 value for slope.

The neural network arrangement for training is shown in Figure 3. With a least error of 0.01, it is clear that during training conditions, the program is effective. For training set ID 1, the gradient remains 0.00048193 in epoch 7, as seen in Figure 5. Figure 5 depicts the regression analysis for R = 0.99977 and for R = 0.99874, respectively.

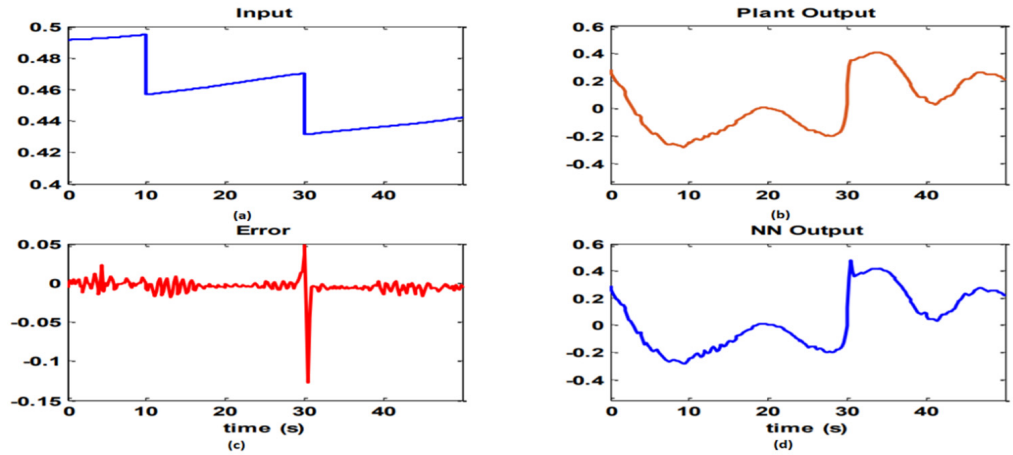

Figure 5. Validation of data using neural network for sample 1, (**a**) actual plant input (*Idin*,*act*), (**b**) actual plant output (*Idout*,*act*), (**c**) controller from actual output to ref. output, (**d**) ANFIS plant ref. output (*Idout*,*ref*).

Iq is simulated in the same way as Id is. By means of PI controllers, data are acquired, and from these data sample 2 was collected. To calculate the errors, the input and output of PI controllers are placed into the data validation area, as shown in Figure 6. Additionally, output side error and neural network output side error are shown in Figure 6. The error

exhibits transients firstly at 4.85 s and then 30 s later due to changes in load and wind speed. Furthermore, the usual range for this is 0.01–0.015. After this, no transition state is seen by 4.85 s and 30 s.

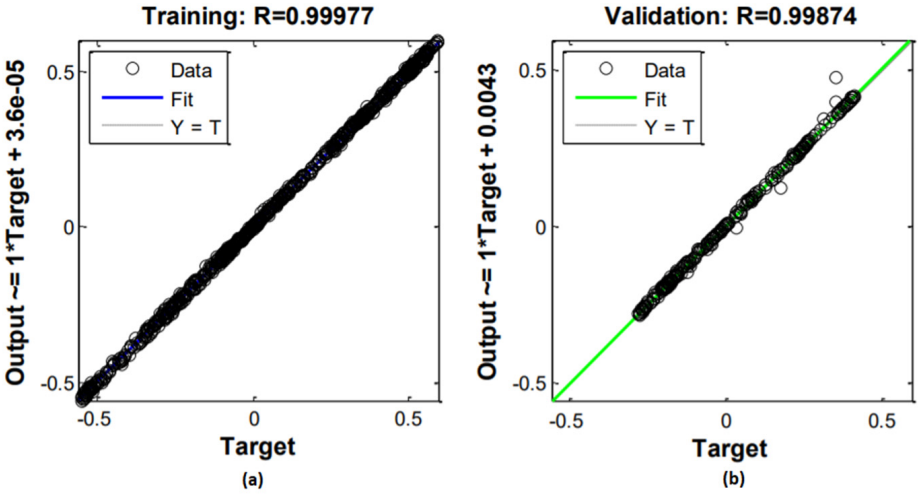

Figure 6. NN regression analysis for sample 1, (**a**) training of ref. and actual with R = 0.99977, (**b**) validation of ref. and actual with R = 0.99874.

The ANFIS controller provided for coordinated control action using DFIG and STATCOM uses two-layer architecture for direct and quadrature axis control axis. In order to train the model, the input error between the actual direct axis current and reference direct axis current has been given as input to train the model with K_p and K_i, which are the weighted constraint to the nodes of the model. Overall, 75% of the data were used to train the model and 25% of the data were used to test the model under different constraints. Data training with neural network structure is shown in Figure 7. The least error of training is equal to 0.01 under training conditions, as seen above. Figure 8 depicts the neural network's training state as gradient and mu. As shown in Figure 8, sample 2 of Iq for the training supports the gradient 1.2044×10^5. This is of epoch 200. Values of R for regression used were R = 0.99983 and R = 0.99972, respectively.

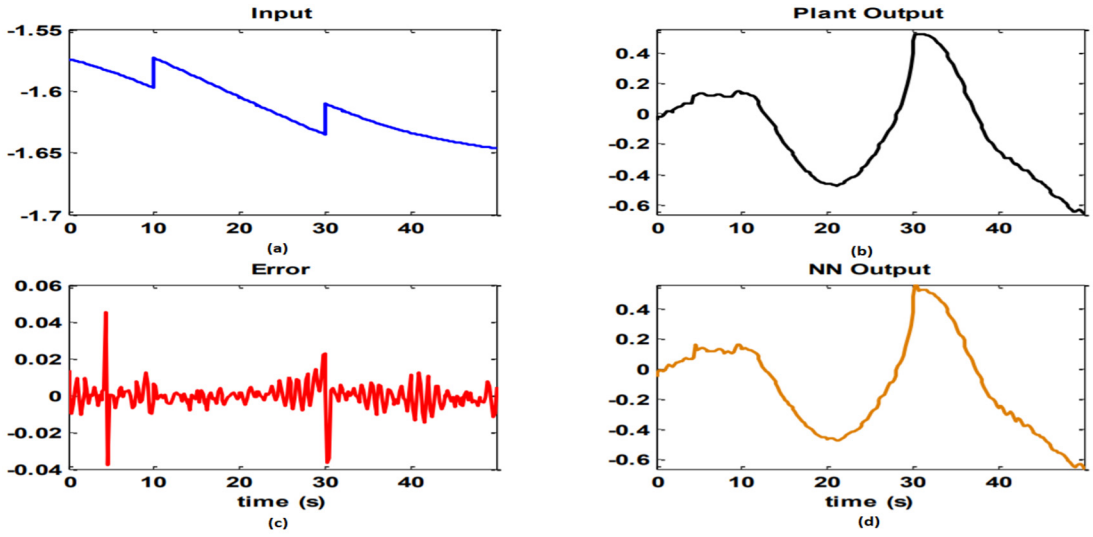

Figure 7. Training of data using neural network for sample 2, (**a**) plant input (*Idin*), (**b**) reference plant output (*Idout*), (**c**) controller from actual output to ref. output, (**d**) ANFIS plant output (*Idout*,*t*).

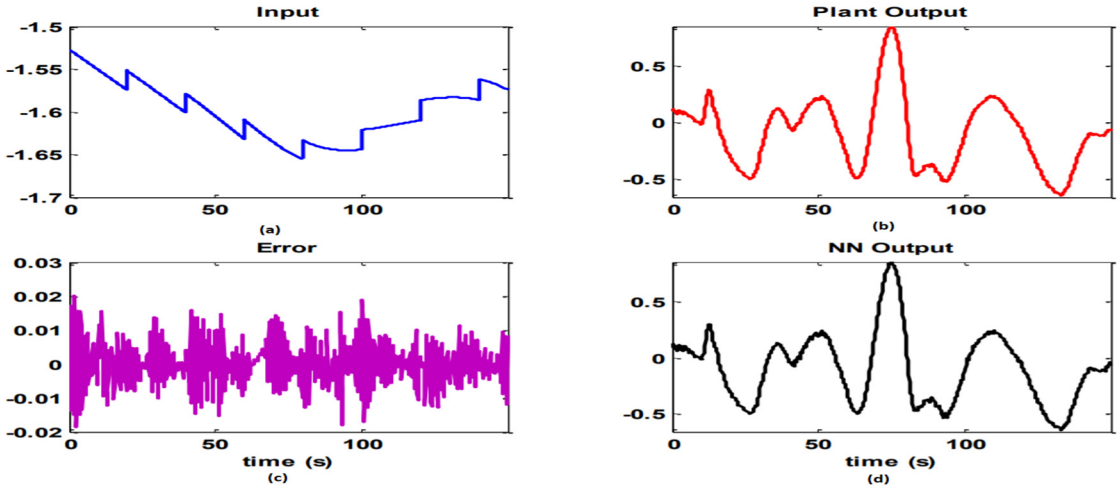

Figure 8. Validation of data using neural network for sample 2, (**a**) actual plant input (*Idin*,*t*), (**b**) actual plant output (*Idout*,*act*), (**c**) controller from actual output to ref. output, (**d**) ANFIS plant ref. output (*Idout*,*ref*).

The method used is the gradient descent to gather samples from the controllers' output and input to further reduce the error. The trial is considered to be on samples 3 and 4. To detect the errors, the input and output data of PI controller for IDs were provided to the data validator, as shown Figure 9 shows the NN regression analysis for sample 2, where Figure 9a is training of ref. and actual with R = 0.99983, and Figure 9b represents the validation of ref. and actual with R = 0.99972. The training data set for sample 3 is shown at Figure 10. Similarly, Figure 11 Shows the validation of data using neural network for sample 3. The error indicates transient behavior after around 30 s due to load variations, and it also demonstrates that the error range is normally 0.001 to 0.001, excluding transient I which is up to 30 s.

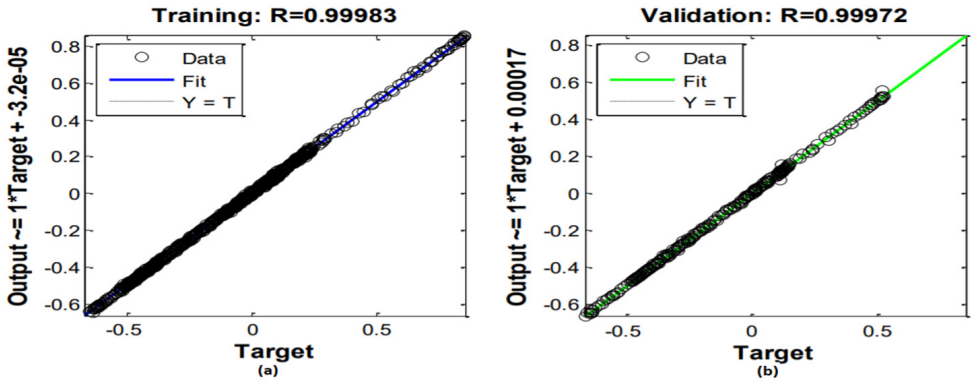

Figure 9. NN regression analysis for sample 2, (**a**) training of ref. and actual with R = 0.99983, (**b**) validation of ref. and actual with R = 0.99972.

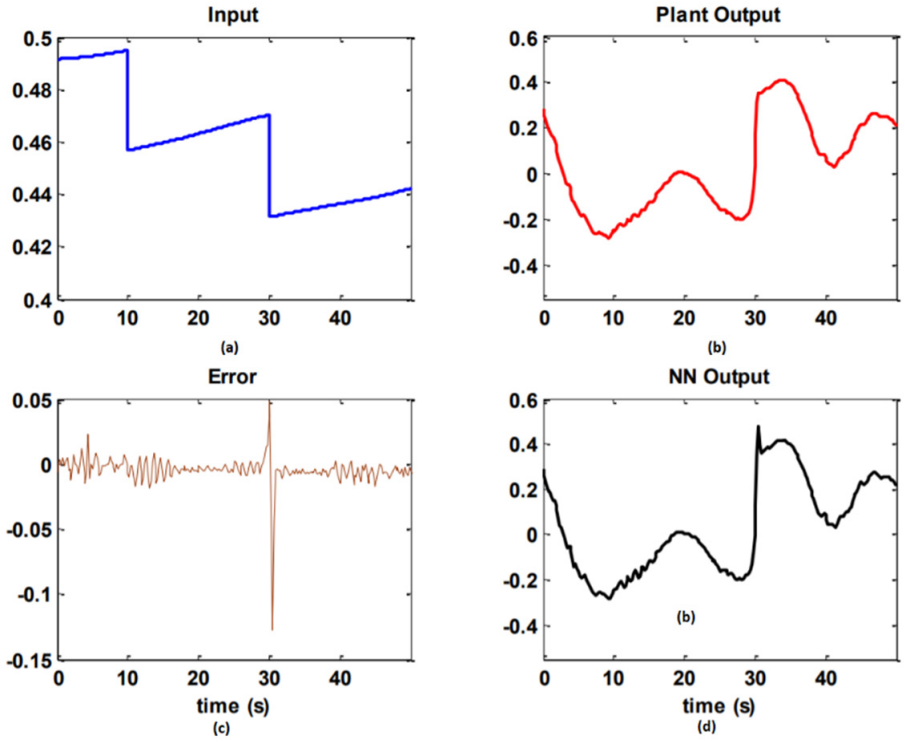

Figure 10. Training of data using neural network for sample 3, (**a**) plant input (*Idin*), (**b**) reference plant output (*Idout*,*ref*), (**c**) controller from actual output to ref. output, (**d**) ANFIS plant output (*Idout*,*act*).

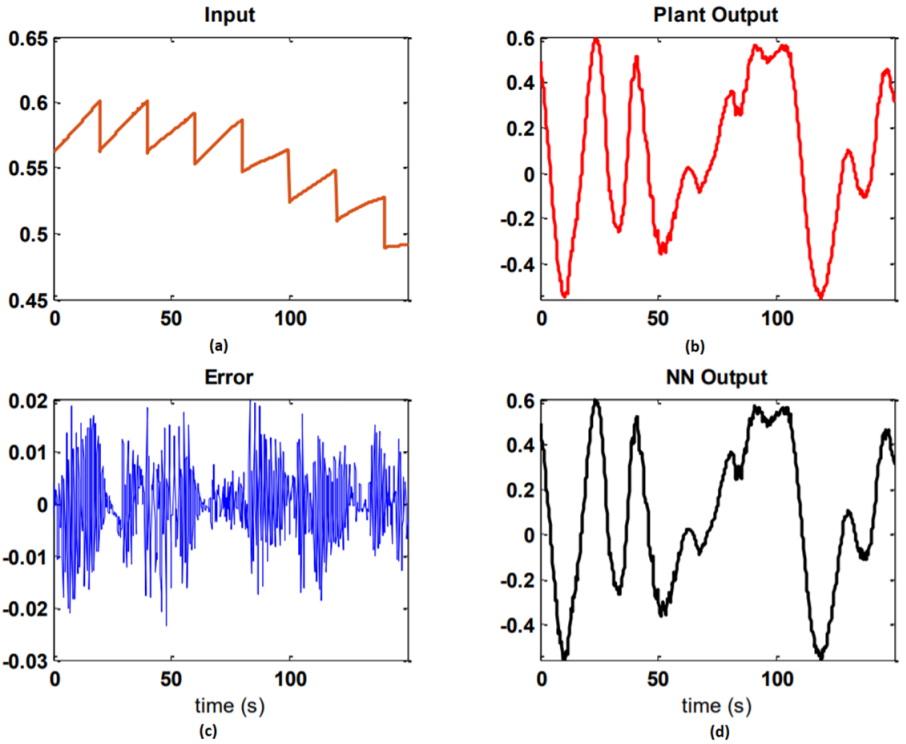

Figure 11. Validation of data using neural network for sample 3, (**a**) actual plant input (*Idin*,*t*), (**b**) actual plant output (*Idout*,*act*), (**c**) controller from actual output to ref. output, (**d**) ANFIS plant ref. output (*Idout*,*ref*).

The best four samples, similar to sample 2, have been examined, and the same will be used for the SA-PI controller in Section 5 [45,46].

The NN regression analysis for sample 3, has been presented at Figure 12. Here the training and testing has been done for 0.999 and 0.998 respectively. Again for sample 4 the training and validation is shown at Figures 13 and 14 respectively. Figure 15 represents the NN regression analysis for sample 4 with training and validation value of 0.996 and 0.997 respectively.

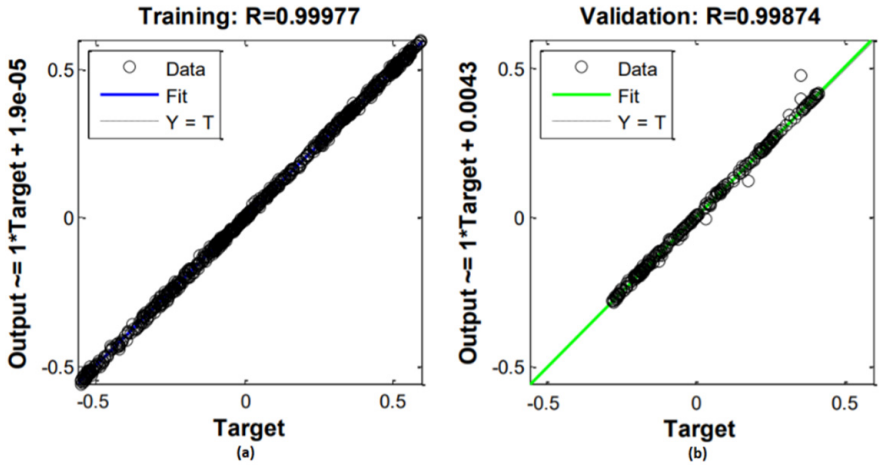

Figure 12. NN regression analysis for sample 3, (**a**) training of ref. and actual with R = 0.99977, (**b**) validation of ref. and actual with R = 0.99874.

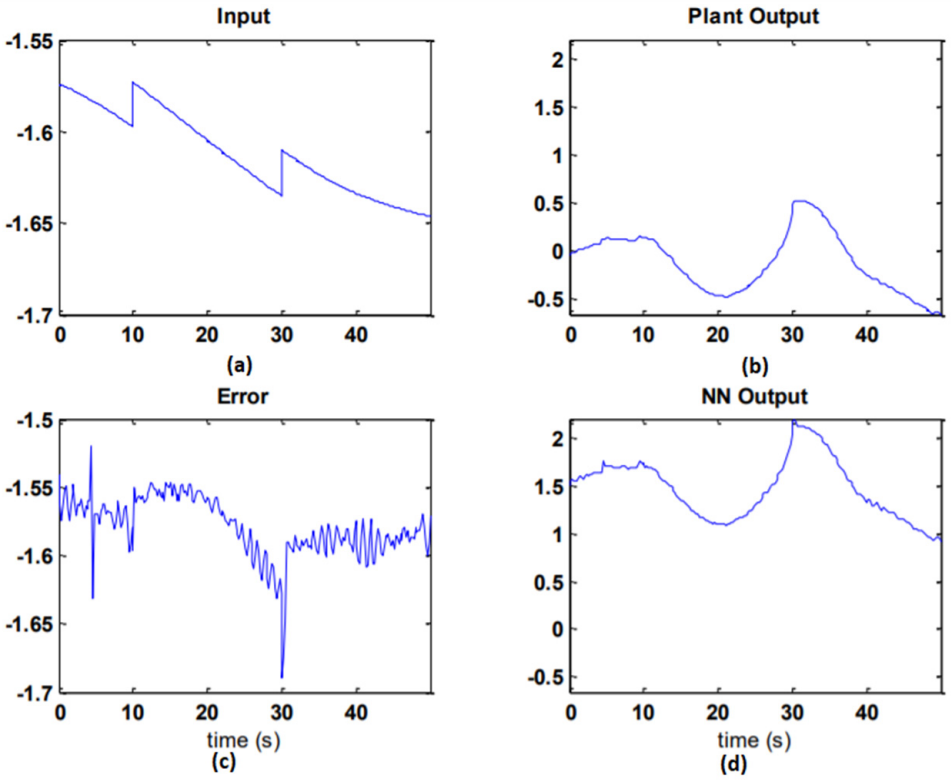

Figure 13. Training of data using neural network for sample 4, (**a**) plant input (*Idin*), (**b**) reference plant output (*Idout*), (**c**) controller from actual output to ref. output, (**d**) ANFIS plant output (*Idout*,*t*).

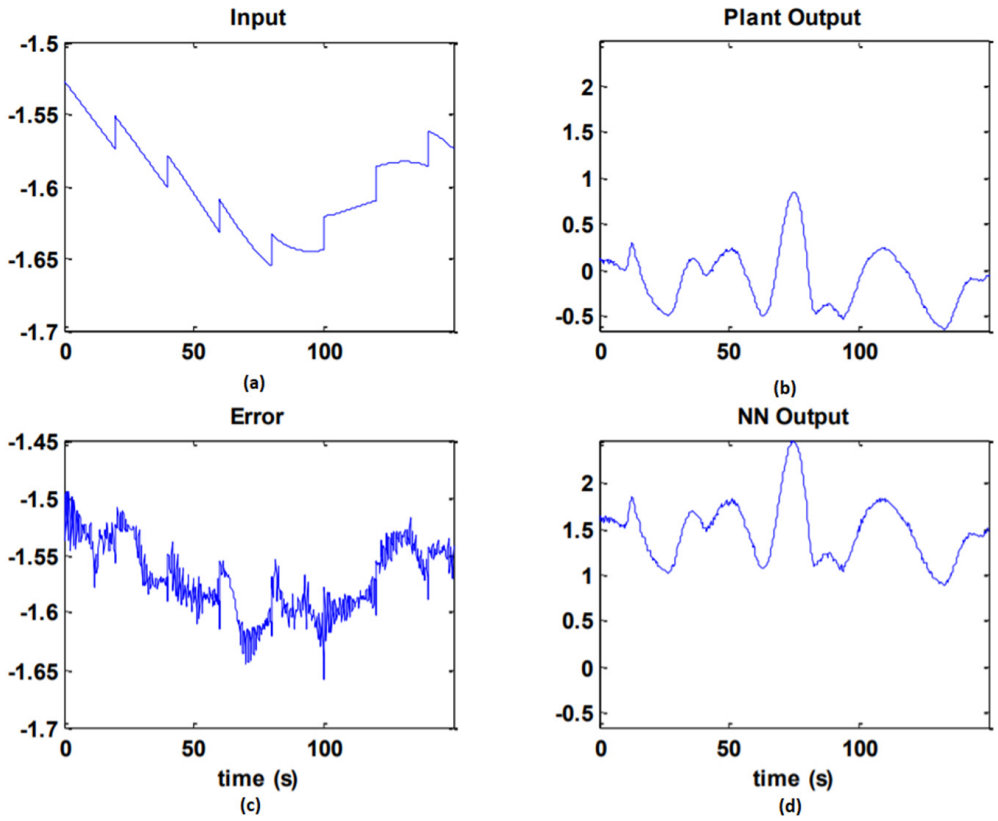

Figure 14. Validation of data using neural network for sample 4, (**a**) actual plant input (*Idin*,*t*), (**b**) actual plant output (*Idout*,*act*), (**c**) controller from actual output to ref. output, (**d**) ANFIS plant ref. output (*Idout*,*ref*).

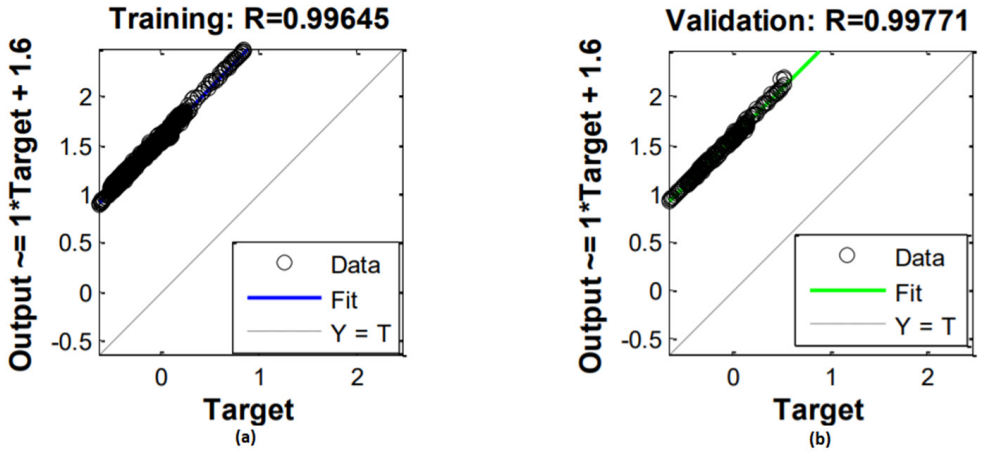

Figure 15. NN regression analysis for sample 4, (**a**) training of ref. and actual with R = 0.99645, (**b**) validation of ref. and actual with R = 0.99771.

4.2. Case-II

The procedure starts with two-step results. These are two parallel FPA (flower pollination algorithm) solutions that will be built into the main algorithm to determine the 5-fold cross authentication and best higher parameter estimate. The following are some of the crucial steps in the procedure:

1. Set the value of time t = 0 and start the FPA (flower pollination algorithm) and parallel algorithm.
2. Between the two data sets of data, evaluate similarity and the pollen distance.

3. In pollen space, evaluate the flatness in FPA from the range 0.3 to 0.99.
4. With reference to decision variables, check for global and local optimization.
5. Set the outcome to stopping criterion once Gbest is attained.
6. For the training and for testing sets, make two databases.
7. If the best possible solution is not receiving, change the Gaussian surface.

The investigation of multiple FPA (flower pollination algorithms) Gaussian models to enhance the parameter of controller is shown in Tables 1 and 2. With the FPA optimization, stratified analysis was performed, although the best result was reported here for 0.95 band width (GBW). We looked at different forms of Gaussian surfaces for analysis. Table 2 shows that for sigma 0.8, the three Gaussian surfaces have identical RMSE, value of response time, and RF attributes to the GBW = 0.95.

Table 1. Different Gaussian model analysis with GBW = 0.95.

Sigma	Type of Gaussian Surface	RMSE	Response Time	RF
0.8	Squared Exponential	1.7723	3.77	9.4
	Matern 5/2 GPR	1.7179	3.72	17.7
	Exponential GPR	1.4233	3.52	6.43
0.9	Squared Exponential	1.581	3.08	9.3
	Matern 5/2 GPR	1.647	3.17	11.4
	Exponential GPR	1.292	3.10	4.77
0.94	Squared Exponential	1.782	3.7	9.45
	Matern 5/2 GPR	1.8798	3.2	9.3
	Exponential GPR	1.5653	3.2	7.13

Table 2. Analysis of different Gaussian models with GBW = 0.96.

Sigma	Type of Gaussian Surface	RMSE	Response Time	RF
0.8	Squared Exponential	1.7723	3.77	9.4
	Matern 5/2 GPR	1.9179	3.72	17.7
	Exponential GPR	1.4233	3.57	6.43
0.9	Squared Exponential	1.717	3.324	9.267
	Matern 5/2 GPR	1.129	3.213	11.217
	Exponential GPR	1.328	2.96	4.8
0.94	Squared Exponential	1.782	3.78	9.45
	Matern 5/2 GPR	1.8208	3.205	9.092
	Exponential GPR	1.4865	3.224	7.248

5. Result Analysis

In the problem formulation section, it has been discussed that the mathematical model satisfies the secondary condition of the rotor side controller and that of the STATCOM controller. Therefore, RMSProp-PI Controller was used to design the coordinated control between dfig and STATCOM. As the proposed problem is nonconvex, therefore, LSTM-enabled RMSProp-PI was designed using the Matlab Simulink model as per Appendix A, where the optimality has been derived by Python programming for different boundary value conditions. The model also tested various feasibility and safety concerns associated with the different types of faults, such as line 2 ground fault, line to line to ground fault, and triple line to ground fault.

Before starting the analysis for different types of faults, it was required to define the RMSProp and LSTM boundary conditions for different types of uncertainties, the response time, and the fault clearance time in the memory of LSTM. The classical approach for tuning the experimental parameter setup can be analyzed for different values of static boundary value conditions; however, this method will not solve the problem during non-convex optimization. In order to solve the problem using RMSProp and LSTM, the following conditions have been assumed before the modeling using Matlab Simulink. Each function has to be differentiable from the curve over the curve and produce a boundary gradient such

that the corresponding stochastic gradient is bounded. The simulation design parameter is shown in Table 3.

Table 3. Simulation design parameter.

Sl. No.	Parameters	Rating
1	Grid Voltage	400 V, 50 Hz
2	Line Parameters	1 ohm, 1 mH
3	Coupling Inductor	3 mH, 0.5 ohm
4	DC Bus Capacitor	1.34 mH
5	Vdc, Ref. Voltage	700 V
6	Sampling Time	2×10^{-6} s
7	Switching Frequency	15 kHz

5.1. Case-1: Single Line to Ground Fault

The IEEE 5 bus system has been considered to validate the performance of DFIG and STATCOM under the single line-to-ground fault condition and their coordinated control action to mitigate the transient disturbances by providing enough reactive power to the transmission line. As per the detailed engineering calculation, a fault at 3.2 km away from a wind turbine has been identified as the place for a single line to ground fault. The minimum fault duration is 0.2 s, and the maximum fault duration is three cycles. The objective is to identify the fault within two cycles and to take corrective measures to rectify the fault within one cycle.

Figure 16 shows the mathematical model and 3D view of the line-to-ground fault situation in the IEEE 5 bus system. The Matlab Simulink-based 3D model represents the hyperplane of the PI controller transfer function. Here, three different curves have been shown as part of the three situations that occur during the fault condition, such as transfer function hyperplane after one cycle as represented by Figure 16a, and after two cycles and three cycles, it is shown in Figure 16b,c, respectively. It is clearly understood that during the fast instant of the fault cycle, the upper boundary is -2, and that of the lower boundary is -4. Similarly, during the second cycle of observation, it is noticed that the upper boundary has increased to 0.00, and that of the lower boundary is at -0.5. The same boundary becomes more constrained for the triple line to ground fault condition.

Figure 16 represents Mathematical model and 3D view of the line-to-ground fault situation for three different cycle of observation. The Figure 17 represents the matplotlib heat function of the optimization window. Here, X-axis represents the proportional gain, and the Y-axis represents integral gain. As stated earlier, optimization has to be carried out to control reactive power flow between the STATCOM and the transmission line. In the figure, that is the optimization using RMSProp converges at 0, and that of the integral controller has a maximum value of 0.42 to track the line to ground fault during transient disturbances. The operation above can be achieved by making the integral controller dynamic oscillate between 0.36 and 0.42. Again, from the heat map, it is also understood that the system is stable in tracking the fault under a predefined contour configuration. Similarly, Figure 17b,c represent the optimization window for the second and third cycles. During the second cycle, a slight deviation in the proportional gain has been noticed, and this is probably due to the line-to-ground fault having a lower impedance.

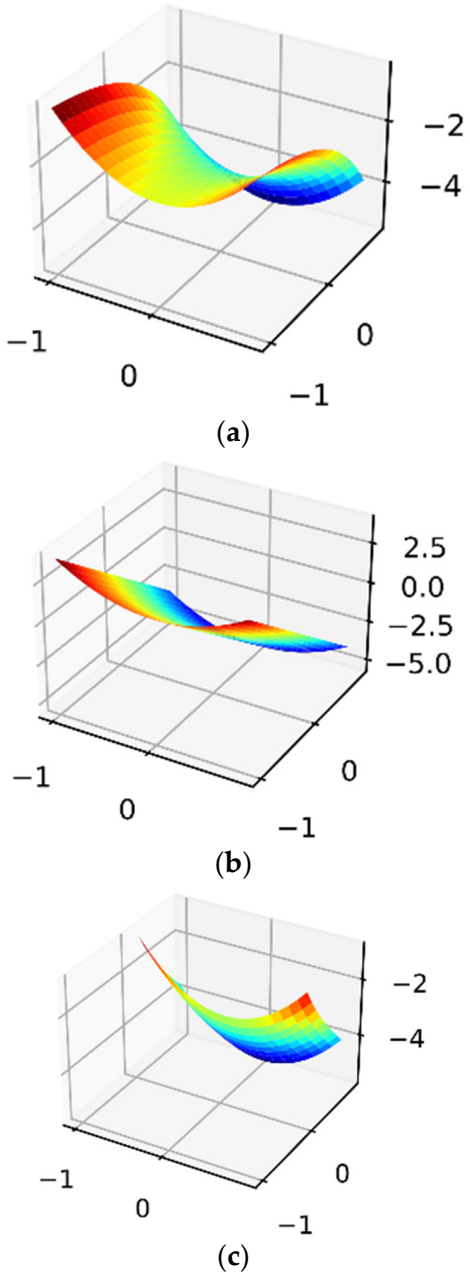

Figure 16. Mathematical model and 3D view of the line-to-ground fault situation. (**a**) First cycle observation of voltage waveform. (**b**) Second cycle observation of voltage waveform. (**c**) Third cycle observation of voltage waveform.

Figure 18 shows the cost optimization for RMSProp with PI controller interms of error analysis and reward. Table 4 represents a comparative analysis between without (Situation 1) and with (Situation 2) coordinated control of different techniques for DFIG and STATCOM. In a IEEE –5 bus system, a detailed comparative analysis between ANFIS-PI, GA-PI, and RMSProp-PI has been carried out. The analysis of real power and reactive power exchange between the STATCOM and the line at various distances from the STATCOM position has been presented. As observed with RMSProp, the system can deliver more power under power compensation mode without and with the coordinated control system. It is also observed that a sharp increase in 3% power delivery capability from without to with a coordinated system for RMSProp. A detailed comparative analysis of the different PI controllers in terms of step response is presented in Table 5.

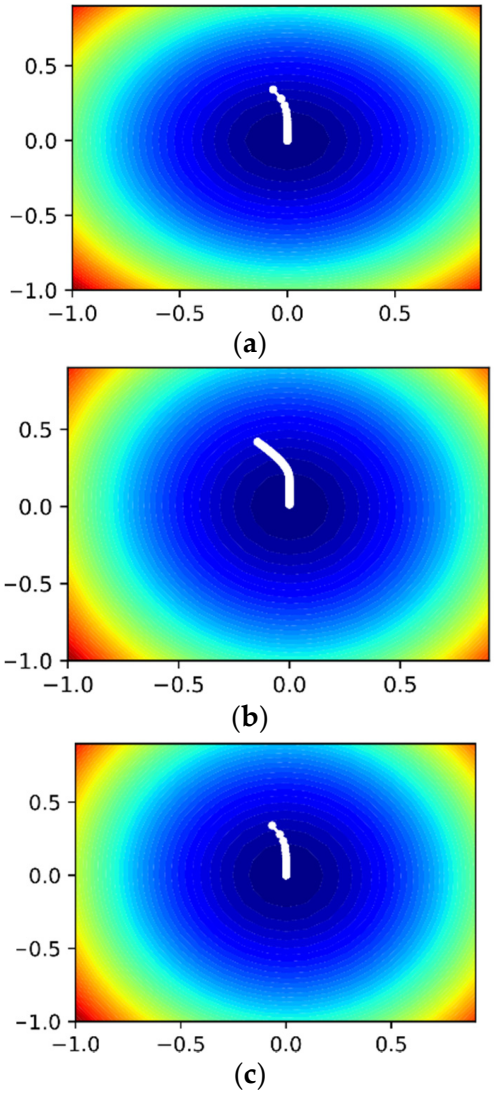

Figure 17. Matplotlib heat function of the optimization window. (**a**) First cycle observation of voltage waveform. (**b**) Second cycle observation of voltage waveform. (**c**) Third cycle observation of voltage waveform.

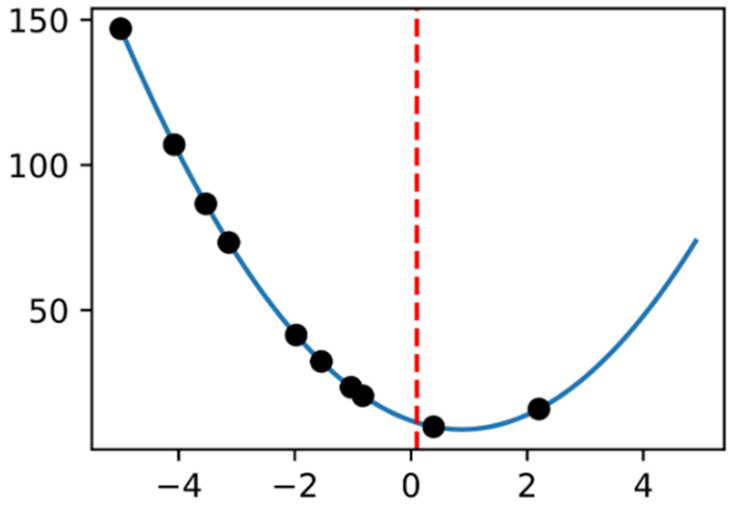

Figure 18. Cost function optimization for RMSProp + PI.

Table 4. Comparative analysis between without and with coordinated control of different techniques for DFIG and STATCOM under line-ground fault.

Bus No.		**1–2**		**1–4**		**2–3**		**3–5**		**4–5**	
STATCOM Distance from Tr. Line		**1.45**		**2.07**		**3.41**		**4.22**		**4.67**	
		P	Q	P	Q	P	Q	P	Q	P	Q
Without Coordinated Control Between DFIG and STATCOM	ANFIS + PI	0.015	0.044	0.058	0.061	0.449	0.150	0.022	0.024	0.029	0.031
	FPA + PI	0.014	0.041	0.054	0.057	0.42	0.14	0.021	0.022	0.027	0.029
	RMSProp + PI	0.016	0.047	0.062	0.066	0.483	0.161	0.024	0.025	0.031	0.033
With Coordinated Control Between DFIG and STATCOM	ANFIS + PI	0.015	0.044	0.058	0.062	0.454	0.151	0.023	0.024	0.029	0.031
	FPA + PI	0.016	0.048	0.063	0.066	0.485	0.162	0.024	0.026	0.031	0.033
	RMSProp + PI	0.017	0.051	0.067	0.071	0.522	0.174	0.026	0.027	0.033	0.036

Table 5. Comparative analysis of the different PI controllers in terms of step response.

System Type	**Parameters**	**Proportional Gain**	**Integral Gain**	**Rise Time**	**Peak Time**	**Settling Time**	**Max over Shoot**
Situation 1	ANFIS + PI	0.32	0.57	0.88	0.97	1.2	11.24
	FPA + PI	0.29	0.57	0.83	0.99	1.4	11.007
	RMSProp + PI	0.36	0.70	1.02	1.20	1.66	13.48
Situation 2	ANFIS + PI	0.38	0.68	1.05	1.15	1.43	13.38
	FPA + PI	0.35	0.68	0.99	1.18	1.67	13.10
	RMSProp + PI	0.43	0.83	1.21	1.43	1.98	16.04

Figure 19 represents the step response of the RMSProp-PI controller supported by LSTM. It is observed that the estimated system response initially behaves transiently up to one second, and after that, the system becomes undammed against the original system performance under damping in nature after one second. This shows that the proposed controller is more robust in tracking the fault and initiating corrective measures to rectify the system as soon as possible. Similarly, Figure 20 represents the DC voltage reference of STATCOM where, due to control action, the system shows minor disturbances at one second and 1.5 s, respectively. Similarly, the real and reactive power exchange at the point of STATCOM and GSC is shown in Figure 21. Similarly Figure 22 represents Initial transient real power between STATCOM and line.

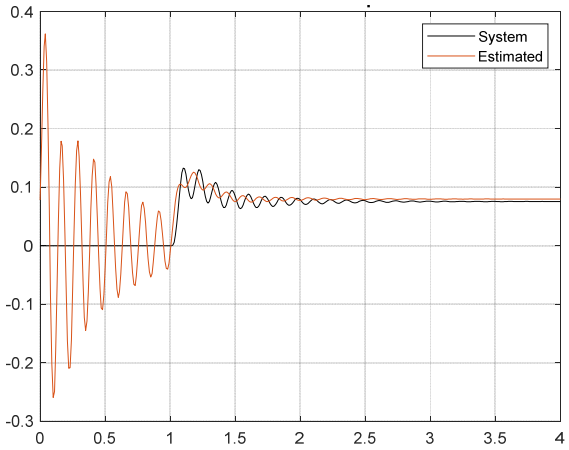

Figure 19. Step response of RMSProp + PI controller supported by LSTM.

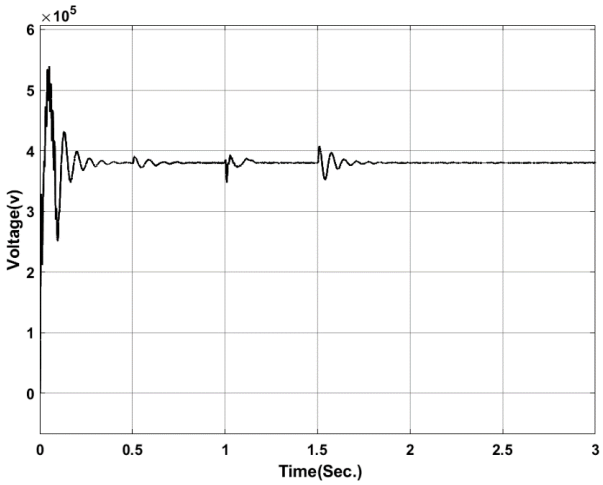

Figure 20. DC reference voltage of STATCOM.

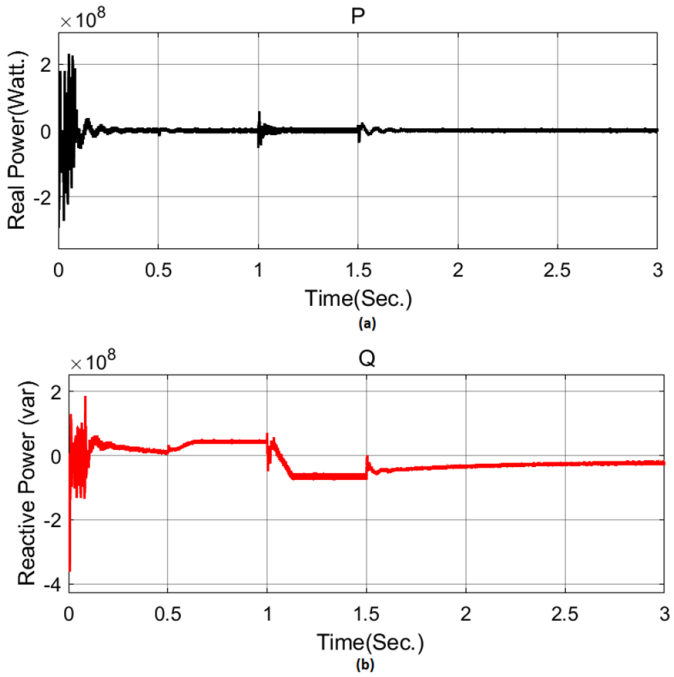

Figure 21. (**a**) Real power at the pcc of STATCOM and GSC under SLG. (**b**) Reactive power at the pcc of STATCOM and GSC under SLG.

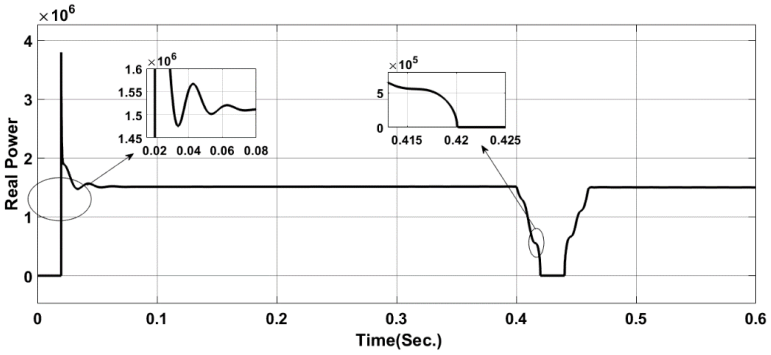

Figure 22. Initial transient real power between STATCOM and line.

5.2. Case-2: Line-Line to Ground Fault

The occurrence of the double line to ground fault is about 66% as compared to the single line to ground fault. This requires a robust Pi controller to achieve the coordinated control action between the DFIG and that of STATCOM. Two different types of stability analysis, such as minor signal disturbance and significant signal disturbance, have been investigated with two different tolerance levels. The mathematical model and the 3D view of the line-to-ground fault situation are shown in Figure 23.

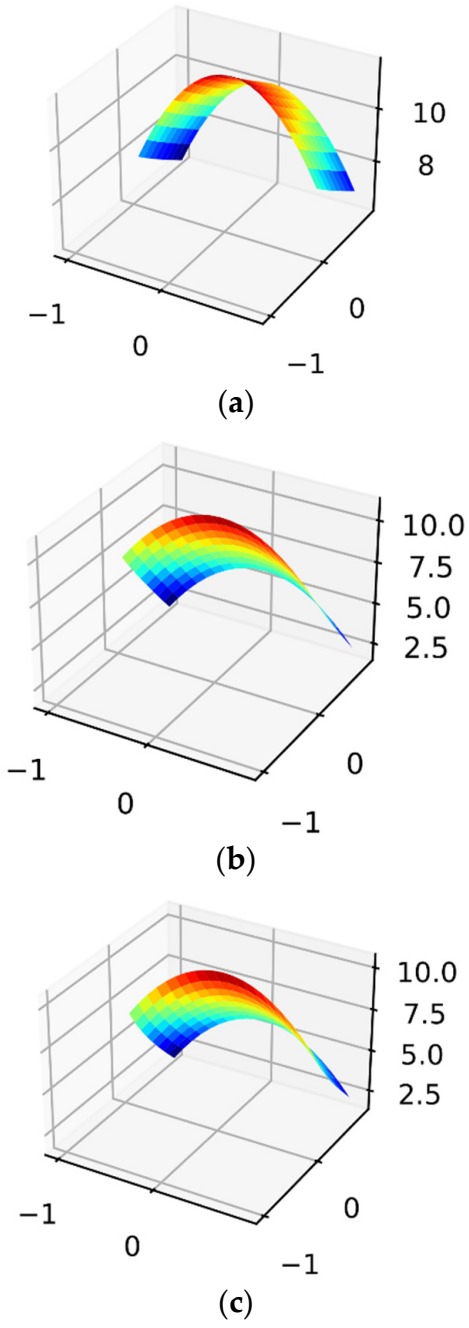

Figure 23. Mathematical model and 3D view of the line-line-to-ground fault situation. (**a**) First cycle observation of voltage waveform. (**b**) Second cycle observation of voltage waveform. (**c**) Third cycle observation of voltage waveform.

The Matlab Simulink-based 3D model represents the hyperplane of the PI controller transfer function. Here, three different curves have been shown as part of the three

situations that occur during the fault condition, such as transfer function hyperplane after one cycle as represented by Figure 23a, and after two cycles and three cycles, it is shown in Figure 23b,c respectively. It is clearly understood that during the fast instant of the fault cycle, the upper boundary is 10.01, and that of the lower boundary is 7.61. Similarly, during the second cycle of observation, it is noticed that the upper boundary has decreased to 8.24, and that of the lower boundary is at 2.5 with a left-hand side slope of 1.17. Again, in the third cycle of observation, it is noticed that the upper boundary has reduced to 7.5, and that of the lower boundary is at 1.91 with a left-hand side slope of 1.03.

Figure 24 represents the matplotlib heat function of the optimization window. In the figure, it is clear that that is the optimization using RMSProp converges at 0, and that of the integral controller has a maximum value of 0.44 to track the line-line to ground fault during transient disturbances. The operation above can be achieved by making the integral controller dynamic oscillate between 0.39 and 0.44. Again, from the heat map, it is also understood that the system is approaching towards unstable while tracking the fault under a predefined contour configuration from the second cycle onwards. Similarly Figure 25. Shows the cost function optimization for RMSProp + PI.

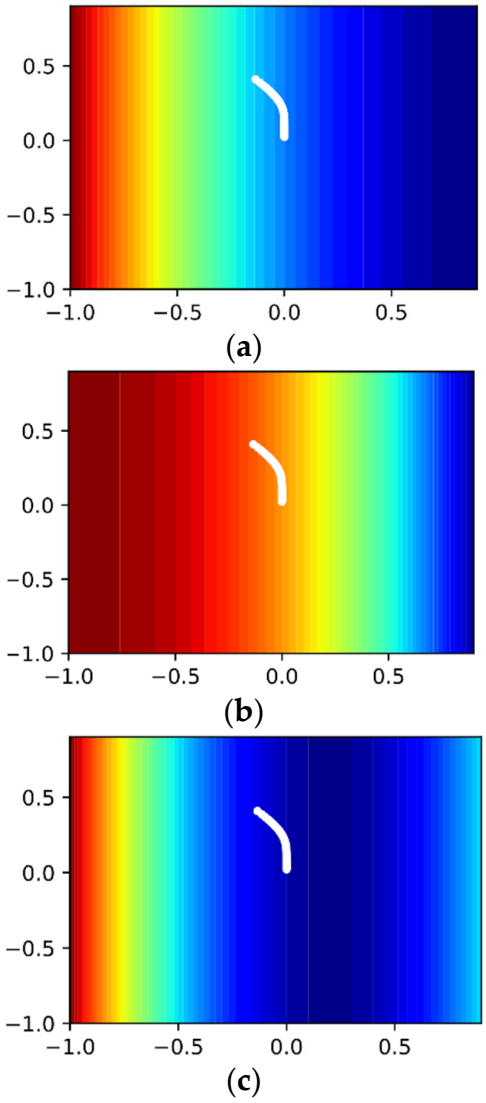

Figure 24. Matplotlib heat function of the optimization window. (**a**) First cycle observation of voltage waveform. (**b**) Second cycle observation of voltage waveform. (**c**) Third cycle observation of voltage waveform under line-line-ground fault.

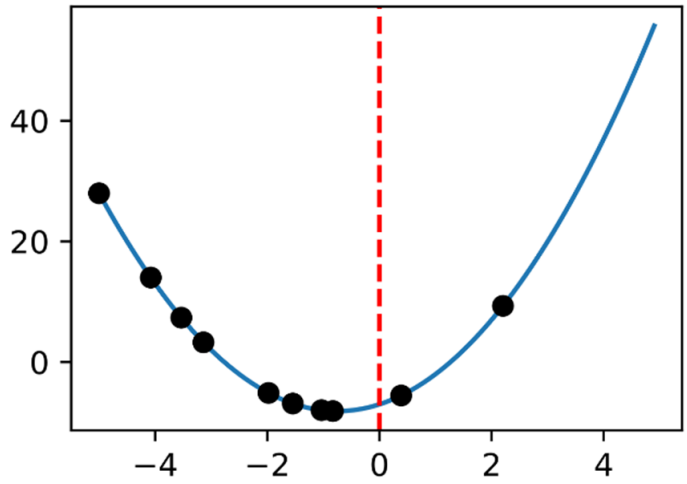

Figure 25. Cost function optimization for RMSProp + PI.

Table 6 represents a comparative analysis between without (Situation 1) and with (Situation 2) coordinated control of different techniques for DFIG and STATCOM. As observed with RMSProp, the system can deliver more power under power compensation mode without and with the coordinated control system. It was also observed that, due to the line-line-ground fault, a decrease in the power delivery of 23.2% occurs from without to with a coordinated system for RMSProp. A detailed comparative analysis of the different PI controllers in terms of step response has been presented in Table 7.

Table 6. Comparative analysis between without and with coordinated control of different techniques for DFIG and STATCOM under line-line-ground fault.

Bus No.		**1–2**		**1–4**		**2–3**		**3–5**		**4–5**	
STATCOM Distance from Tr. Line		**1.45**		**2.07**		**3.41**		**4.22**		**4.67**	
		P	Q	P	Q	P	Q	P	Q	P	Q
Without Coordinated Control Between DFIG and STATCOM	ANFIS + PI	0.012	0.035	0.046	0.048	0.355	0.119	0.017	0.019	0.023	0.024
	FPA + PI	0.011	0.032	0.043	0.045	0.332	0.111	0.017	0.017	0.021	0.023
	RMSProp + PI	0.013	0.037	0.049	0.052	0.382	0.127	0.019	0.020	0.024	0.026
With Coordinated Control Between DFIG and STATCOM	ANFIS + PI	0.012	0.035	0.046	0.049	0.359	0.119	0.018	0.019	0.023	0.024
	FPA + PI	0.013	0.038	0.050	0.052	0.383	0.128	0.019	0.021	0.024	0.026
	RMSProp + PI	0.013	0.040	0.053	0.056	0.412	0.137	0.021	0.021	0.026	0.028

Table 7. Comparative analysis of the different PI controllers in terms of step response under line-line-ground fault condition.

System Type	**Parameters**	**Proportional Gain**	**Integral Gain**	**Rise Time**	**Peak Time**	**Settling Time**	**Max over Shoot**
Situation 1	ANFIS + PI	0.37	0.67	1.03	1.13	1.40	13.15
	FPA + PI	0.34	0.67	0.97	1.16	1.64	12.88
	RMSProp + PI	0.42	0.82	1.19	1.40	1.94	15.77
Situation 2	ANFIS + PI	0.41	0.73	1.12	1.23	1.53	14.32
	FPA + PI	0.37	0.73	1.06	1.26	1.79	14.02
	RMSProp + PI	0.46	0.89	1.29	1.53	2.12	17.16

Figure 26 represents the step response of the RMSProp-PI controller supported by LSTM. It was observed that the estimated system response has no initial transient up to one second, and after that, the system became under-damped against the original system performance. Similarly, Figure 27 represents the DC voltage reference of STATCOM, where, due to control action, the system shows major disturbances during the initial stage and at one second and 1.5 s, respectively. Similarly, the real and reactive power exchange at the point of STATCOM and GSC is shown in Figure 28.

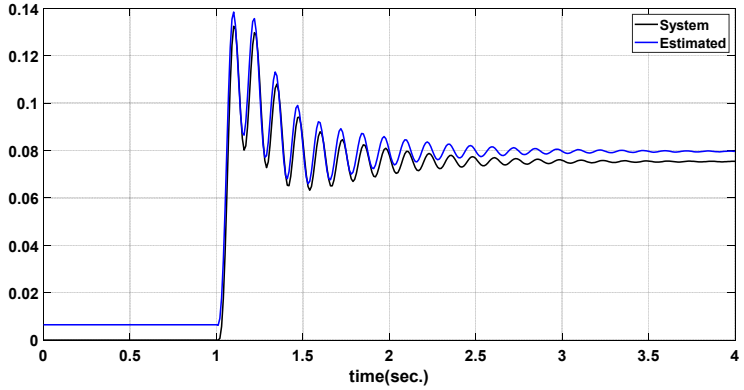

Figure 26. Step response of RMSProp + PI controller supported by LSTM under line-line-ground fault condition.

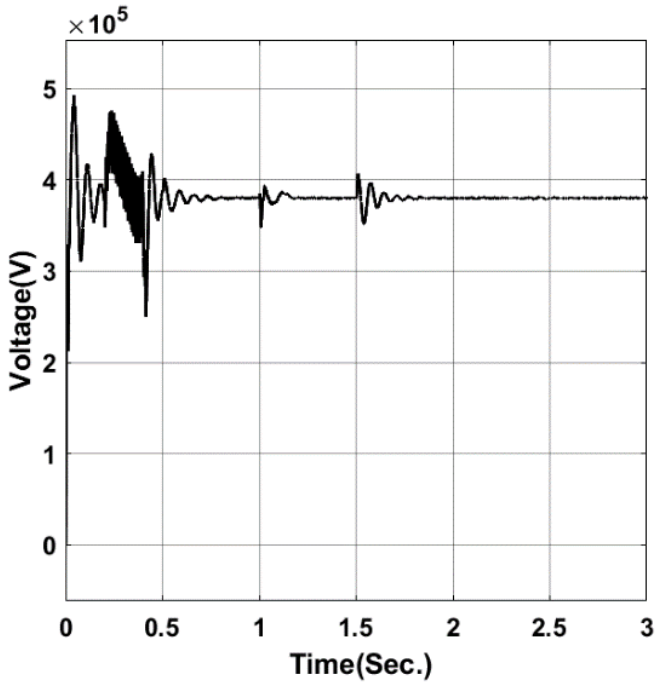

Figure 27. DC reference voltage of STATCOM under line-line-ground fault condition.

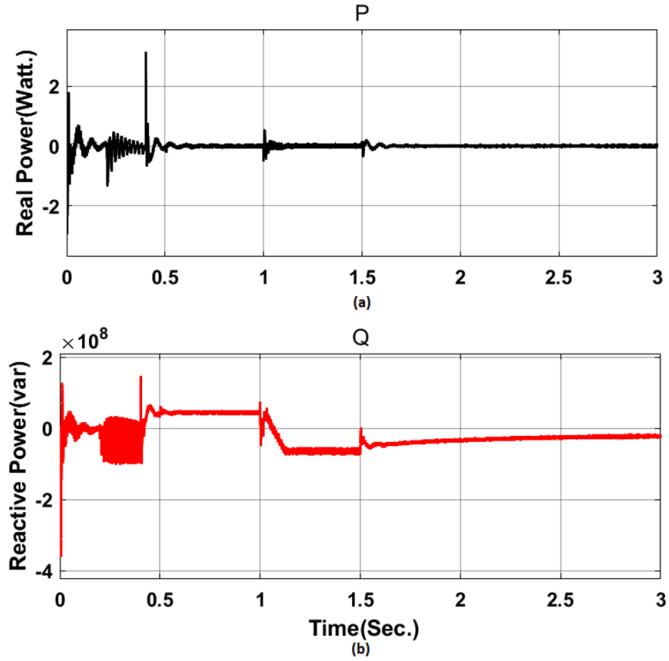

Figure 28. (**a**) Real power at the pcc of STATCOM and GSC under SLG. (**b**) Reactive power at the pcc of STATCOM and GSC under SLG.

5.3. Case-3: Line-Line-Line to Ground Fault

The occurrence of the triple line to ground fault is about 41% compared to the single line to ground fault and 48%. The mathematical model and 3D view of the line-to-ground fault situation is shown in Figure 29.

It is clearly understood from Figure 29 that during the fast instant of the fault cycle, the upper boundary is 11.81, and that of the lower boundary is −0.62. Similarly, during the second cycle of observation, it was noticed that the upper boundary increased to 15.37 with a left-hand side slope and that of the lower boundary was at −1.81 with a left-hand side slope of 4.36. Again, in the third cycle of observation, it was noticed that the upper boundary has reduced to 5.62, and that of the lower boundary was −0.97 with a left-hand side slope of −8.57. This shows that the system behaves more transient in its disturbances at the zero crossing point and the severity of the fault.

Figure 30 represents the matplotlib heat function of the optimization window. The operation above can be achieved by making the integral controller dynamic oscillate between −0.12 and 0.38. Again, from the heat map, it is also understood that system is approaching towards being unstable while tracking the fault under a predefined contour configuration from the second cycle onwards. Figure 31 shows the cost function optimization for RMSProp + PI.

Table 8 represents a comparative analysis between without (Situation 1) and with (Situation 2) coordinated control of different techniques for DFIG and STATCOM under triple line to ground fault. It was observed that, due to triple line-ground fault, a decrease in power delivery of 37.66% occurs from without to with a coordinated system for RMSProp. A detailed comparative analysis of the different PI controllers, in terms of step response, is presented in Table 9.

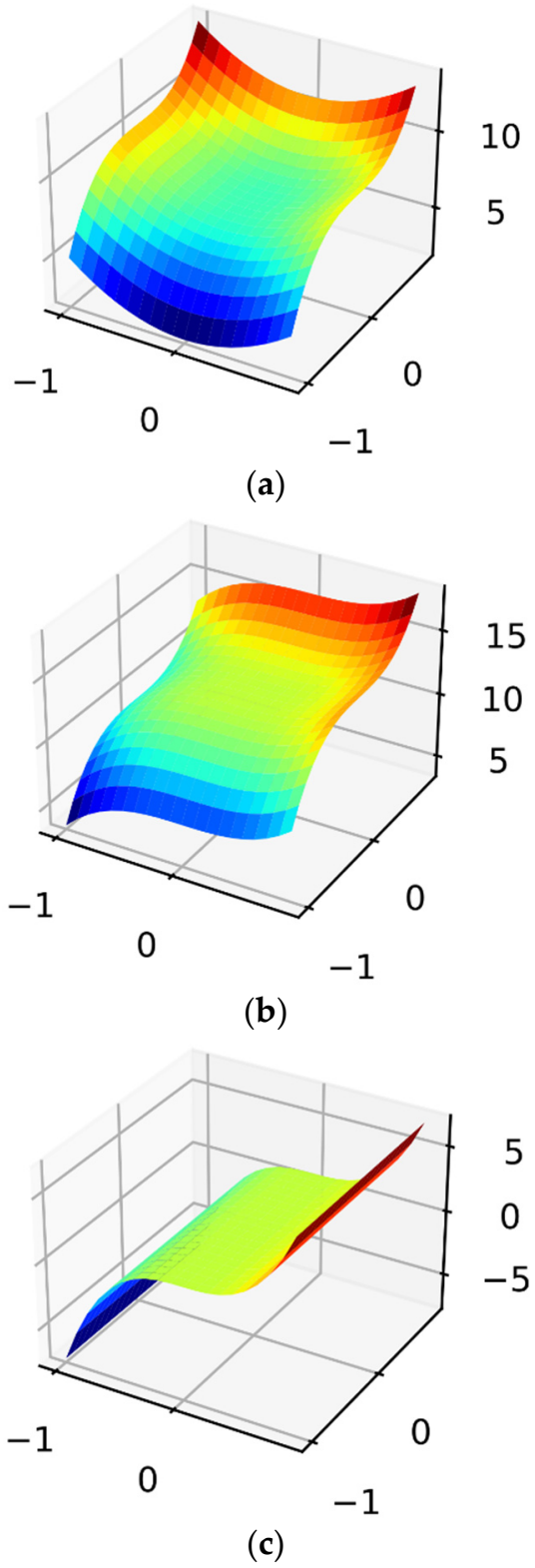

Figure 29. Mathematical model and 3D view of the triple line-to-ground fault situation. (**a**) First cycle observation of voltage waveform. (**b**) Second cycle observation of voltage waveform. (**c**) Third cycle observation of voltage waveform under line-line-ground fault.

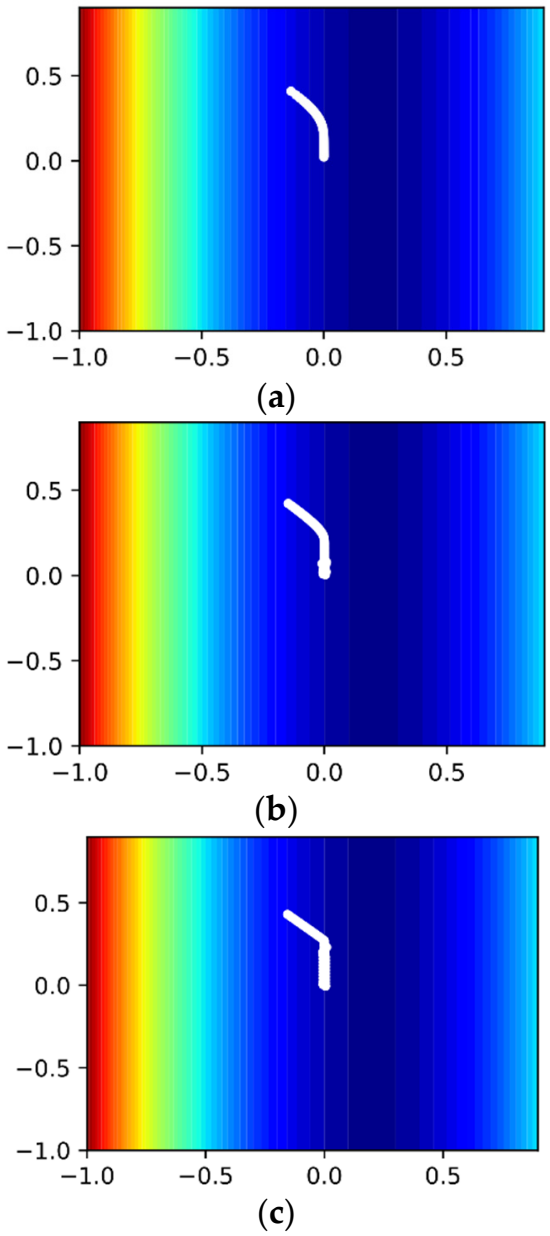

Figure 30. Matplotlib heat function of the optimization window for triple line to ground fault. (**a**) First cycle observation of voltage waveform. (**b**) Second cycle observation of voltage waveform. (**c**) Third cycle observation of voltage waveform under line-line-ground fault.

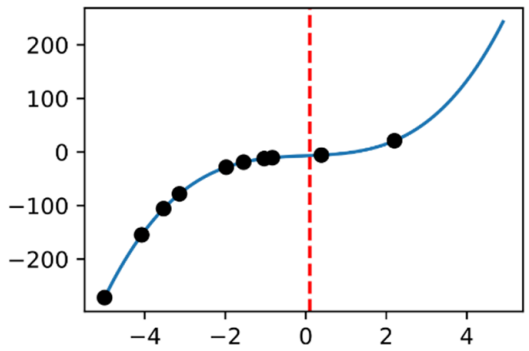

Figure 31. Cost function optimization for RMSProp + PI.

Table 8. Comparative analysis between without and with coordinated control of different techniques for DFIG and STATCOM under triple-line-ground fault.

Bus No.		**1–2**		**1–4**		**2–3**		**3–5**		**4–5**	
STATCOM Distance from Tr. Line		**1.45**		**2.07**		**3.41**		**4.22**		**4.67**	
		P	Q	P	Q	P	Q	P	Q	P	Q
Without Coordinated Control Between DFIG and STATCOM	ANFIS + PI	0.011	0.031	0.041	0.043	0.319	0.107	0.016	0.017	0.021	0.022
	FPA + PI	0.010	0.029	0.038	0.040	0.298	0.099	0.015	0.016	0.019	0.021
	RMSProp + PI	0.011	0.033	0.044	0.047	0.343	0.114	0.017	0.018	0.022	0.023
With Coordinated Control Between DFIG and STATCOM	ANFIS + PI	0.011	0.031	0.041	0.044	0.322	0.107	0.016	0.017	0.021	0.022
	FPA + PI	0.011	0.034	0.045	0.047	0.344	0.115	0.017	0.018	0.022	0.023
	RMSProp + PI	0.012	0.036	0.048	0.050	0.371	0.124	0.018	0.019	0.023	0.026

Table 9. Comparative analysis of the different PI controllers in terms of step response under line-line-ground fault condition.

System Type	**Parameters**	**Proportional Gain**	**Integral Gain**	**Rise Time**	**Peak Time**	**Settling Time**	**Max over Shoot**
Situation 1	ANFIS + PI	0.49	0.89	1.37	1.50	1.86	17.49
	GA + PI	0.45	0.89	1.29	1.54	2.18	17.13
	RMSProp + PI	0.56	1.09	1.58	1.86	2.58	20.97
Situation 2	ANFIS + PI	0.55	0.97	1.49	1.64	2.03	19.05
	GA + PI	0.49	0.97	1.41	1.68	2.38	18.65
	RMSProp + PI	0.61	1.18	1.72	2.03	2.82	22.82

Figure 32 represents the DC voltage reference of STATCOM, where due to control action, the system shows major disturbances during the initial stage and at one second and 1.66 s, respectively. Similarly, the real and reactive power exchange at the point of STATCOM and GSC is shown in Figure 33.

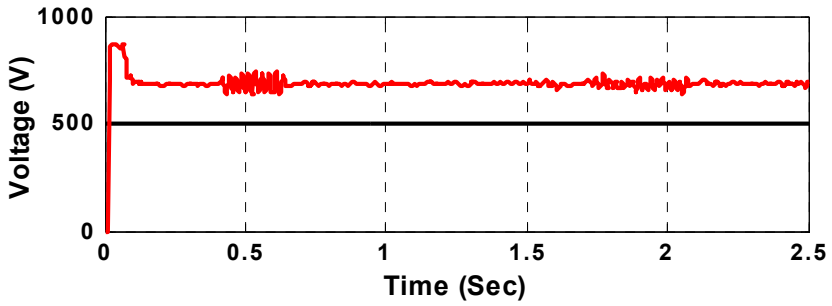

Figure 32. DC reference voltage of STATCOM under line-line-ground fault condition.

The ANFIS-based PI controller changes the parameters Kp and Ki according to the changes in the power system operating condition at the time of disturbance. ANFIS is a combination of neural network with fuzzy interference system, which is a branch of artificial intelligence characterized by fuzzification, defuzzification, and rule base. Fuzzy logic deals with linguistic variables and neural networks, requiring input and output databases for training. Generally, for linear databases, the back propagation network is used, and for nonlinear databases, the multilayer feed forward neural network is preferred. The output of PI controller is set as target for the process of production and for the final stage of the

neural network training and replicating model. Triangular membership functions here are used as parameters. The in-feed and result variables of the controller are constructed using the five membership functions of NL, ZE, PL, NS, and PS. They are used as language variables. During training, these parameters were trained at intervals of 10 epoch. A standard PI controller was used here to process the parameters Id and Iq. This output of the controller was given to the first layer, and it converts this to a crisp variable. Five membership functions (MFs) were employed in the current model. Taking reference from MF, the back propagation technique was used to estimate various types of two weights (w1 and w2). The normalization property was utilized to turn the same into a second level of crisp variable. It was then converted back to an initial physical variable at the end of layer 5 using addition operation.

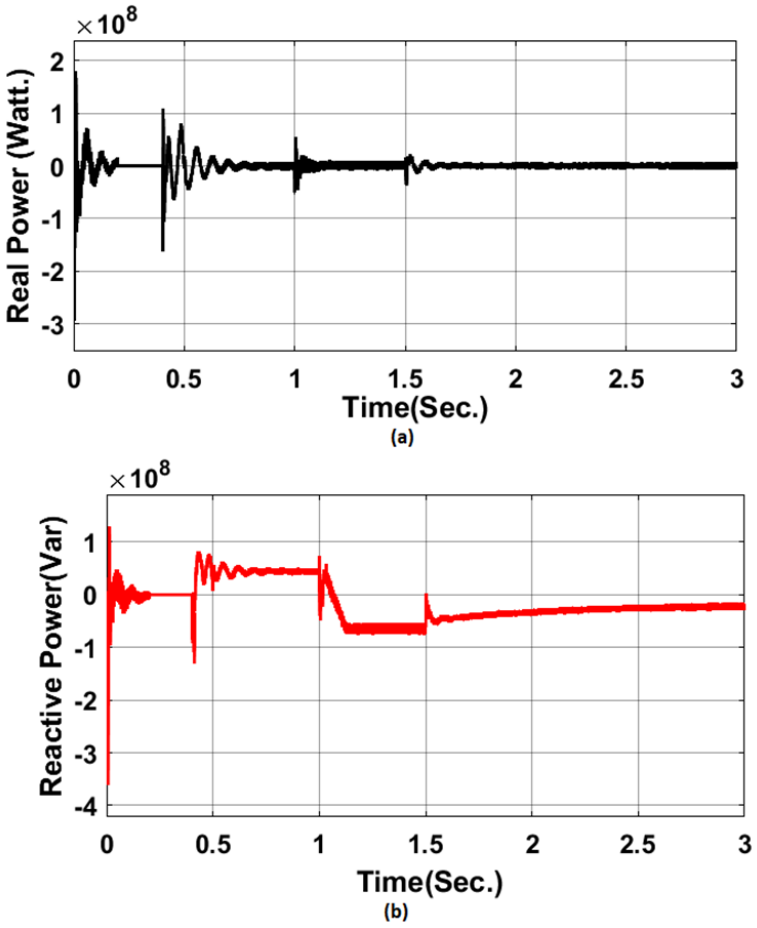

Figure 33. (**a**) Real power at the pcc of STATCOM and GSC under SLG. (**b**) Reactive power at the pcc of STATCOM and GSC under SLG.

From the simulation in MATLAB/SIMULINK, it was observed that proposed ANFIS is comparable to conventional PI controller and PI plus FLC to increase the stability of the system. The suggested ANFIS system is learned from the studied system's transient responses with the proposed STATCOM in combination with developed Fuzzy plus PI controller, and the device responses, along with the proposed STATCOM in conjunction with the ANFIS, provide a better output response. We can say that STATCOM and ANFIS achieve steady state values and the system's transient responses are the quickest. This says that the proposed STATCOM with ANFIS controller will provide the studied device with sufficient reactive power and improve the damping characteristics to easily dampen the intrinsic oscillations of the tested system against the tested system without a controller with a PI and a PID plus fuzzy controller.

6. Conclusions

Coordinated control among DFIG and STATCOM using ANFIS, FPA, and RMSProp has been established in the present research paper. A detailed comparative analysis has been presented among the methodologies. As observed, the coordinated control strategies work well under conditions such as the faulted distance from the substation, which should not be more than 3 km from the STATCOM vicinity, with a minimum allowable fault resistance of 0.18 ohm for the ANFIS and FPA-based control systems. The NN-error, as obtained from the experiment under case-2 of benchmarking model, was observed to be 0.99982. This is almost close to the reference line passing through the origin. Although ANFIS shows better performance in predicting the situation, from a stability point it was not found to be suitable.

In the IEEE-5 bus test system, the STATCOM has been connected between bus no. 2–3 for one experiment and in between 3–5 in the second experiment. From Table 7, it can be observed that, without coordinated control, the power exchange between the bus 2–3 becomes 0.343 kwatt and 0.114 kvar for RMSprop and that of 0.298 kwatt and 0.099 kvar for FPA + PI has been achieved. With coordinated control, it increased to 0.371 kwatt and 0.124 kvar for RMSprop.

A detailed stability analysis for the line to line to ground fault was presented in Table 8. It was found that RMSProp + PI controller provides a maximum overshoot of 17.49% as compared to 20.97% in ANFIS + PI controller under situation 1. Similarly, under situation 2 it was 19.05% and 22.82%, respectively.

Author Contributions: Conceptualization, R.R.H.; Data curation, R.D.; Formal analysis, R.R.H.; Funding acquisition, D.C.; Investigation, R.D.; Methodology, K.J.R.; Resources, K.J.R.; Supervision, S.K.M.; Validation, R.D.; Writing—review & editing, V.S. and D.C. All authors have read and agreed to the published version of the manuscript.

Funding: This research received no external funding.

Institutional Review Board Statement: Not applicable.

Informed Consent Statement: Not applicable.

Data Availability Statement: Not applicable.

Acknowledgments: The authors would like to thank the School of EEE, REVA University, Bengaluru, GHRU, Amravati and VIT, Vellore for providing necessary laboratory facility for carrying out the Experiment.

Conflicts of Interest: The authors declare no conflict of interest.

Appendix A

Table A1. Power flow in five bus system without FACTS controller.

Sl. No.	Bus No.	Real Power Flow (P.U)	Reactive Power Flow (P.U)
01.	1–2	0.0142	0.0419
02.	2–4	0.0541	0.0570
04.	4–4	0.4202	0.1402
04.	4–5	0.0210	0.0220
05.	4–5	0.0277	0.0290

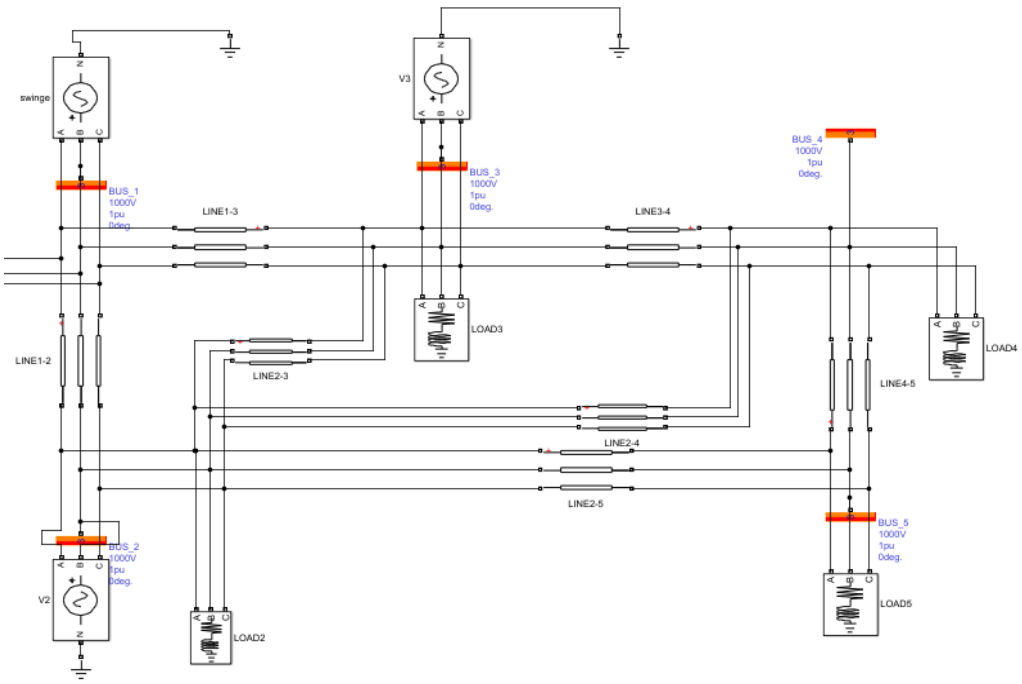

Figure A1. Matlab Simulink of IEEE-5 bus system.

References

1. Chen, X.; Wu, W.; Gao, N.; Chung, H.S.-H.; Liserre, M.; Blaabjerg, F. Finite Control Set Model Predictive Control for LCL-Filtered GridTied Inverter with Minimum Sensors. *IEEE Trans. Ind. Electron.* **2020**, *67*, 9980–9990. [CrossRef]
2. Hingorani, N.G. High Power Electronics and Flexible AC Transmission System. *IEEE Power Eng. Rev.* **1988**, *7*, 3–4. [CrossRef]
3. Parizad, A.; Kalantar, M.; Khazali, A. Application of HSA and GA in Optimal Placement of FACTS Devices Considering Voltage Stability and Losses. In Proceedings of the International Conference on Electric Power and Energy Conversion Systems, Sharjah, United Arab Emirates, 10–12 November 2009; pp. 1–7.
4. Rajderkar, V.P.; Chandrakar, V.K. Comparison of Series FACTS Devices Via Optimal Location in a Power System for Congestion Management. In Proceedings of the 2009 Asia-Pacific Power and Energy Engineering Conference, Wuhan, China, 27–31 March 2009; pp. 1–5.
5. Kheirizad, I.; Mohammadi, A.; Varahram, M.H. A Novel Algorithm for Optimal Location of FACTS Devices in Power System Planning. *J. Electr. Eng. Technol.* **2008**, *3*, 177–183. [CrossRef]
6. Zhang, W.; Li, F.; Tolbert, L.M. *Optimal Allocation of Shunt Dynamic Var Source SVC and STATCOM: A Survey*; Department of Electrical and Computer Engineering, The University of Tennessee: Knoxville, TX, USA, 2006; pp. 1–6.
7. Hete, R.R.; Mishra, S.K.; Dash, R.; Ballaji, A.; Subburaj, V.; Reddy, K.J. Analysis of DFIG-STATCOM P2P control action using simulated annealing techniques. *Heliyon* **2022**, *8*, e09008. [CrossRef] [PubMed]
8. Das, M.C.; Dash, R.; Swain, S.C.; Subburaj, V. Performance Enhancement of PI-Controller Using SVM for DFIG-Grid Interconnected System. In Proceedings of the 2021 2nd International Conference for Emerging Technology (INCET), Belagavi, India, 21–23 May 2021; pp. 1–6. [CrossRef]
9. Palaniraj, P.; Sakthivel, G. Hybrid Motion Estimation Algorithm Based on PSO with Dynamic Threshold on Static Block Detection. *Procedia Comput. Sci.* **2018**, *132*, 1487–1496. [CrossRef]
10. Saurabh, S.; Ahmed, M.I. Optimal Placement of STATCOM for improving voltage stability using GA. *Int. J. Sci. Eng. Technol.* **2014**, *2*, 1349–1353.
11. Karthikeyan, K.; Dhal, P.K. Investigation of optimal location and tuning of STATCOM by genetic algorithm based transient stability improvement. *J. Electr. Syst.* **2018**, *14*, 103–117.
12. Mishra, S.; Dash, R.; Swain, S.C. Line to Ground fault analysis of DFIG and STATCOM using Simulated Annealing optimization-Part-I. In Proceedings of the 2021 International Conference on Innovative Practices in Technology and Management (ICIPTM), Noida, India, 17–19 February 2021; pp. 94–98. [CrossRef]
13. Das, A.; Dawn, S.; Gope, S. A Review on Optimal Placement of FACTS Devices. *Int. J. Comput. Intell. IoT* **2019**, *2*, 626–630.
14. Molinas, M.; Suul, J.A.; Undeland, T. Low voltage ride through of wind farms with cage generators: STATCOM versus SVC. *IEEE Trans. Power Electron.* **2008**, *23*, 1104–1117. [CrossRef]
15. Nguyen, H.V.; Cao, M.T.; Nguyen, H.; Le, K.H. Performance Comparison between PSO and GA in Improving Dynamic Voltage Stability in ANFIS Controllers for STATCOM. *Eng. Technol. Appl. Sci. Res.* **2019**, *9*, 4863–4869. [CrossRef]

16. Ganesh, A.; Dahiya, R.; Singh, G.K. Development of simple technique for STATCOM for voltage regulation and power quality improvement. In Proceedings of the 2016 IEEE International Conference on Power Electronics Drives and Energy Systems (PEDES), Trivandrum, India, 14–17 December 2016; pp. 1–6.
17. Varshney, S.; Srivastava, L.; Pandit, M. Optimal placement and sizing of STATCOM for voltage security enhancement using PSO-TVAC. In Proceedings of the International Conference on Power and Energy Systems, Chennai, India, 22–24 December 2011; pp. 1–6.
18. Saravanan, M.; Slochanal, S.M.R.; Venkatesh, P.; Abraham, J.P.S. Application of particle swarm optimization technique for optimal location of FACTS devices considering cost of installation and system loadability. *Int. J. Electr. Power Syst. Res.* **2007**, *77*, 276–283. [CrossRef]
19. Laifa, A.; Boudour, M. Facts allocation for power system voltage stability enhancement using MOPSO. In Proceedings of the 5th International Multi-Conference on Systems, Signals and Devices, Amman, Jordan, 20–22 July 2008; pp. 1–6.
20. Jena, R.; Swain, S.C.; Dash, R. Power flow simulation & voltage control in a SPV IEEE-5 bus system based on SVC. *Mater. Today Proc.* **2021**, *39*, 1934–1940. [CrossRef]
21. Dash, R.; Paikray, P.; Swain, S.C. Active power filter for harmonic mitigation in a distributed power generation system. In Proceedings of the 2017 Innovations in Power and Advanced Computing Technologies (i-PACT), Vellore, India, 21–22 April 2017; pp. 1–6. [CrossRef]
22. Pattanaik, D.; Mishra, S.; Khuntia, G.P.; Dash, R.; Swain, S.C. An innovative learning approach for solar power forecasting using genetic algorithm and artificial neural network Open Engineering. *Open Eng.* **2020**, *10*, 630–641. [CrossRef]
23. Paul, R.; Dash, R.; Swain, S.C. Design & Analysis of Current Controller for SPV Grid Connected System through Hysteresis CCT. In Proceedings of the 2018 International Conference on Applied Electromagnetics, Signal Processing and Communication (AESPC), Bhubaneswar, India, 22–24 October 2018; pp. 1–6. [CrossRef]
24. Shivani Mishra, R.K. Viral, Integration Phenomena of Renewable Energy with Contemplation of Issues from Electricity Distribution Utility and Consumer Perceptive. In Proceedings of the 2021 International Conference on Sustainable Energy and Future Electric Transportation (SEFET), Hyderabad, India, 21–23 January 2021; pp. 1–6.
25. Pattanaik, D.; Dash, R.; Swain, S.C. A Review on Solar Thermal PV Modeling & Its Characteristics. In Proceedings of the 2018 International Conference on Applied Electromagnetics, Signal Processing and Communication (AESPC), Bhubaneswar, India, 22–24 October 2018; pp. 1–6. [CrossRef]
26. Nsengimana, C.; Han, X.Y.; Li, L.-L. Comparative Analysis of Reliable, Feasible, Low-Cost Photovoltaic Microgrid for a Residential Load in Rwanda. *Int. J. Photoenergy* **2020**, *2020*, 8855477. [CrossRef]
27. Pattanaik, D.; Dash, R.; Swain, S.C. Design & Analysis of Hybrid PSPS with SPV under Islanding Mode of Operation. In Proceedings of the 2018 International Conference on Applied Electromagnetics, Signal Processing and Communication (AESPC), Bhubaneswar, India, 22–24 October 2018; pp. 1–5. [CrossRef]
28. Khan, M.J.; Yadav, A.K.; Mathew, L. Techno economic feasibility analysis of different combinations of PV-Wind-Diesel-Battery hybrid system for telecommunication applications in different cities of Punjab, India. *Renew. Sustain. Energy Rev.* **2017**, *76*, 577. [CrossRef]
29. Mishra, S.; Pattanaik, D.; Pau, R.; Dash, R.; Swain, S.C. A Review on Different Types of Maximum Power Point Tracking System & its Application with PR Current Control Technique. In Proceedings of the 2018 International Conference on Applied Electromagnetics, Signal Processing and Communication (AESPC), Bhubaneswar, India, 22–24 October 2018; pp. 1–6. [CrossRef]
30. Tobias, R.R.; Mital, M.E.; Lauguico, S.; Guillermo, M.; Naidas, J.R.; Lopena, M.; Dizon, M.E.; Dadios, E. Design and Construction of a Solar Energy Module for Optimizing Solar Energy Efficiency. In Proceedings of the 2020 IEEE 12th International Conference on Humanoid, Nanotechnology, Information Technology, Communication and Control, Environment, and Management (HNICEM), Manila, Philippines, 3–7 December 2020; pp. 1–6.
31. Swain, S.C.; Gogoi, A.; Sharma, S.; Dash, R.; Acharya, A. Some Aspects of Fuzzy Logic Controller for Designing MPPT Based SPV System. In Proceedings of the 2018 International Conference on Recent Innovations in Electrical, Electronics & Communication Engineering (ICRIEECE), Bhubaneswar, India, 27–28 July 2018; pp. 3357–3361. [CrossRef]
32. Bernard, M.; Musilek, P. Ant-based optimal tuning of PID controllers for load frequency control in power systems. In Proceedings of the 2017 IEEE Electrical Power and Energy Conference (EPEC), Saskatoon, SK, Canada, 22–25 October 2017; pp. 1–6.
33. Paul, R.; Dash, R.; Swain, S.C. A Comparative Analysis of Pi and Anfis Pi Based Current Control Technique for Three Phase Grid Connected Solar PV System. In Proceedings of the 2018 3rd International Conference on Communication and Electronics Systems (ICCES), Coimbatore, India, 15–16 October 2018; pp. 303–307. [CrossRef]
34. Abhishek, A.; Akbar, S.A. Linear and nonlinear control strategy for full bridge buck converter. In Proceedings of the 2015 International Conference on Electrical, Electronics, Signals, Communication and Optimization (EESCO), Visakhapatnam, India, 24–25 January 2015; pp. 1–6.
35. Singh, S.; Swain, S.C.; Dash, R.; Roy, P. Current control strategies for SPV grid interconnection based on artificial neural network. In Proceedings of the 2017 Innovations in Power and Advanced Computing Technologies (i-PACT), Vellore, India, 21–22 April 2017; pp. 1–5. [CrossRef]
36. Carrasco, J.M.; Franquelo, L.G.; Bialasiewicz, J.T.; Galvan, E.; Guisado, R.C.P.; Prats, M.A.M.; Leon, J.I. Power-Electronic Systems for the Grid Integration of Renewable Energy Sources: A Survey. *IEEE Trans. Ind. Electron.* **2006**, *53*, 1002–1016. [CrossRef]

37. Swain, S.C.; Mishra, S.; Dash, R.; Nanda, G. Performance analysis of different types of PV testing using MATLAB. In Proceedings of the 2017 Innovations in Power and Advanced Computing Technologies (i-PACT), Vellore, India, 21–22 April 2017; pp. 1–6. [CrossRef]
38. Steimer, P.K. Enabled by high power electronics—Energy efficiency renewables and smart grids. In Proceedings of the Power Electronics Conference (IPEC) 2010 International, Sapporo, Japan, 21–24 June 2010; pp. 11–15.
39. Singh, S.; Dash, R.; Roy, P.; Swain, S.C. Performance analysis of a renewable grid interconnected system based on fuzzy logic. In Proceedings of the 2016 International Conference on Signal Processing, Communication, Power and Embedded System (SCOPES), Paralakhemundi, India, 3–5 October 2016; pp. 1931–1936. [CrossRef]
40. Kelley, J.P.; Wetz, D.A.; Turner, G.K.; Cohen, I. Integration of pulsed loads into a Microgrid architecture. In Proceedings of the Plasma Science (ICOPS) 2013 Abstracts IEEE International Conference, San Francisco, CA, USA, 16–21 June 2013.
41. Dey, S.; Dash, R.; Swain, S.C. Optimal design and feasibility study of renewable hybrid energy systems. In Proceedings of the 2016 International Conference on Emerging Trends in Engineering, Technology and Science (ICETETS), Pudukkottai, India, 24–26 February 2016; pp. 1–6. [CrossRef]
42. Ballaji, A.; Dash, R.; Subburaj, V.; Kalvakurthi, J.R.; Swain, D.; Swain, S.C. Design & Development of MPPT Using PSO with Predefined Search Space Based on Fuzzy Fokker Planck Solution. *IEEE Access* **2022**, *10*, 80764–80783. [CrossRef]
43. Swain, S.C.; Panda, S.; Mahapatra, S. A multi-criteria optimization technique for SSSC based power oscillation damping controller design. *Ain Shams Eng. J.* **2016**, *7*, 553–565. [CrossRef]
44. Ledesma, P.; Usaola, J. Doubly Fed Induction Generator Model for Transient Stability Analysis. *IEEE Trans. Energy Convers.* **2005**, *20*, 388–397. [CrossRef]
45. Ekanayake, B.; Holdsworth, L.; Wu, X.G.; Jenkins, N. Dynamic Modeling of Doubly Fed Induction Generator Wind Turbines. *IEEE Trans. Power Syst.* **2003**, *18*, 803–809. [CrossRef]
46. Lei, Y.; Mullane, A.; Lightbody, G.; Yacamini, R. Modeling of the Wind Turbine with a Doubly Fed Induction Generator for Grid Integration Studies. *IEEE Trans. Energy Convers.* **2006**, *21*, 256–264. [CrossRef]